

The dusty heart of nearby active galaxies

I. From 3D clumpy torus models to physical properties of dust around AGN

S. F. Hönig¹ and M. Kishimoto¹

Max-Planck-Institut für Radioastronomie, Auf dem Hügel 69, 53121 Bonn, Germany

Received June 10, 2009; accepted XXX 00, 2009

ABSTRACT

With the possibilities of high-spatial resolution imaging and spectroscopy as well as infrared (IR) interferometry, the dusty environments of active galactic nuclei (AGN) are now in reach of observations. The presumed optically- and geometrically-thick dusty structure, or “dust torus”, is located around the mid-plane of the nuclear accretion disk, reaching from sub-parsec scales outward to several to tens of parsecs. In a series of papers, we aim for stepping towards characterizing physical properties of the dust torus by combining IR high-resolution observations with 3D radiative transfer models. Our main goals involve constraining the spatial distribution of the dust density, exploring the chemical composition of the dust around the AGN, and studying the structure of the dust cloud distribution.

In this first paper, we introduce an upgrade to our 3-dimensional radiative transfer model of clumpy dust tori. The models are presented as tools to translate classical and interferometric observations into characteristic parameters of the dust distribution. We compare model SEDs for different chemical and grain-size compositions of the dust and find that clouds with standard ISM dust and optical depth $\tau_V \sim 50$ appear in overall agreement with observed IR SEDs. By studying parameter dependencies, it is shown that type 1 AGN SEDs can be used to constrain the radial dust cloud distribution power-law index a , as well as the mean number of clouds along an equatorial line of sight N_0 which characterizes the obscuration. Possible degeneracies with the vertical structure of the torus can be overcome by using interferometric data – either modeling the baseline-dependence or the wavelength-dependence of the visibility. Although type 2 AGN can, in principle, also be used to constrain model parameters, obscuration effects make the analysis more ambiguous. We propose a simple, interferometry-based method to distinguish between “compact” and “extended” radial dust distributions without detailed modeling of the data.

Key words. Galaxies: Seyfert – Galaxies: nuclei – Infrared: galaxies – X-rays: galaxies

1. Introduction

The Unification Scheme of active galactic nuclei (AGN) is relying on a toroidal region filled with molecular gas and dust to explain the observed dichotomy of broad- and narrow-line AGN (Antonucci 1993; Urry & Padovani 1995). The presence of this optically-thick region is well supported by direct and indirect observational evidence. Miller & Antonucci (1983) showed that the narrow emission-line galaxy NGC 1068 shows broad optical emission lines in polarized light, scattered outward from the innermost region which is obscured by the “dust torus”. Several succeeding studies confirmed the presence of a hidden broad-line AGN in many narrow-line objects (e.g. Moran et al. 2000, and references therein). From number statistics of obscured type-2 AGN and non-obscured type-1 AGN as well as from direct observations of the pc-scaled molecular gas in nearby AGN, it is inferred that the torus is not only optically thick but also geometrically thick, with a characteristic scale height $h/r \sim 1$ (e.g. Maiolino & Rieke 1995; Lacy et al. 2004; Martínez-Sansigre et al. 2006; Hicks et al. 2009).

Obscuration of the torus does not only affect the optical broad lines but can also be observed in X-ray and optical/UV continuum emission from the accretion disk and its immediate vicinity. Optically-obscured type-2 AGN are usually associated with high Hydrogen column densities in the X-ray, from

$\sim 10^{23} \text{ cm}^{-2}$ to Compton-thick columns of $> 10^{24-25} \text{ cm}^{-2}$ (e.g. Shi et al. 2006). The material causing these high column densities is generally believed to reside in the dust torus, tracing the gaseous component which dominates the total mass of the torus. Moreover, strong reflection on parsec scales, as observed in the X-ray continuum around 30 keV and associated with large equivalent width of the Fe-K α line, are interpreted as signs for the presence of the torus.

Since a sizable portion of the torus consists of dust, the UV/optical accretion disk emission heats up the dust which thermally re-radiates the received energy in the infrared at temperatures of some 100 K up to the dust sublimation temperature of ~ 1500 K. These temperatures are reached on scales of about 0.1 to 100 pc, depending on the actual AGN luminosity, torus geometry, and dust composition. The thermal radiation from the torus dominates the total near- to mid-infrared (IR) emission of the AGN (“red bump”) with a noticeable cut-off at around $1 \mu\text{m}$ where the UV/optical accretion disk emission starts to dominate (“big blue bump”). At around 10 and $18 \mu\text{m}$, type-1 AGN show some broad spectral features caused by hot silicate dust which is believed to be associated with the inner part of the torus. On the other hand, these silicate features appear in absorption in most type 2 AGN where only cooler dust is seen.

Due to the small spatial scales at which the torus resides, it is a difficult task to directly resolve it by infrared observations. Thus, first reports of successful resolution of the nucleus of an AGN involved interferometric techniques. Wittkowski et al.

Send offprint requests to: S. F. Hönig
e-mail: shoenig@mpifr.de

(1998) used bispectrum speckle interferometry to resolve the nucleus of the Seyfert 2 galaxy NGC 1068 in the K -band, followed-up by additional H -band observations (Weigelt et al. 2004). Swain et al. (2003) presented K -band long-baseline interferometry of the type-1 AGN NGC 4151 which arguably resolve the innermost hot region of the dust torus (see Kishimoto et al. 2007, for this interpretation). More recently, VLTI/MIDI long-baseline mid-IR spectro-interferometry directly revealed the parsec-scaled dust emission sizes in the wavelength band from 8 to $13\mu\text{m}$ for a number of nearby type 1 and type 2 AGN (Jaffe et al. 2004; Tristram et al. 2007; Beckert et al. 2008; Raban et al. 2009; Tristram et al. 2009). These observations finally confirmed the basic picture of the dust torus while more detailed characteristics remain unclear.

The dust torus has been the subject of several kinds of models in order to extract physical properties from broad SED and, in some cases, interferometric observations. Initially, most authors used smooth dust distributions with different kind of radial and vertical density profiles (e.g. Pier & Krolik 1993; Granato & Danese 1994; Efstathiou & Rowan-Robinson 1995; Schartmann et al. 2005). It was, however, early noted that the dust is most probably arranged in clouds instead of being smoothly distributed (e.g. Krolik & Begelman 1988; Tacconi et al. 1994; Hönig & Beckert 2007). This idea received further support by interferometric observations which arguably rule out smooth dust distributions (Jaffe et al. 2004; Tristram et al. 2007). Several radiative transfer models have been developed to account for 2D or 3D clumpy dust distributions (Nenkova et al. 2002; Dullemond & van Bemmelen 2005; Hönig et al. 2006; Schartmann et al. 2008). All of these models appear in more or less good agreement with observations, while the resulting torus or cloud properties differ significantly. Hönig et al. (2006) used optically thick dust clouds and a low torus volume filling factor to simultaneously model near- and mid-IR photometry and interferometry of NGC 1068 (see also Hönig et al. 2007, 2008), while Schartmann et al. (2008) model a torus with high volume filling factor and optically thin clouds for a similar set of observations of the Circinus galaxy. Although the actual properties of the dust clouds are not yet constrained by observations, theoretical predictions and hydrodynamic simulations arguably favor small and compact optically-thick clouds (e.g. Vollmer et al. 2004; Beckert & Duschl 2004; Hönig & Beckert 2007; Schartmann et al. 2009).

This paper series aims at pushing forward our understanding of the physics of AGN dust tori by combining 3D radiative transfer models with high-spatial resolution infrared observations obtained by large telescope-aperture photometry, spectroscopy, and long-baseline interferometry. In this first paper, we present a significant update of our 3-dimensional radiative transfer model of clumpy AGN tori (Hönig et al. 2006). In particular, a better handling of the diffuse radiation field inside the torus has been implemented, and the possibility of different dust compositions and grain sizes is now included. With the upgraded model presented in this paper, we intend to prepare modeling of observational data of the subsequent papers in this series, and try to describe some basic relations among fundamental properties of the dust distribution around the AGN. Some emphasis will be put on the dust grain size and chemical composition which is only marginally explored in literature despite observational evidence that the grain composition might be crucial (e.g. Kishimoto et al. 2007, 2009).

2. Torus model

In this section, we will describe the model principles and underlying assumptions. First, the modeling strategy is outlined and assumptions are explained. Then, we present results of Monte Carlo simulations of dust clouds using different dust compositions. Finally, we introduce the basic “language” and parameters of the torus model.

2.1. Model strategy

The most straight-forward way of modeling clumpy dust tori in 3 dimensions is direct Monte Carlo simulation of a geometrically well-defined, statistically arbitrary distribution of dust clouds spread on a model grid, as demonstrated by Schartmann et al. (2008). There are, however, several technical and practical problems that occur. When solving the radiative transfer equation by Monte Carlo simulations, it is important to properly sample optically thick surface regions by enough grid cells so that each cell is optically thin. Otherwise, emission temperatures will be underestimated leading to a wrong final source function which affects torus SEDs and images. In principle, adaptive grids can be used, but this may become a difficult task when aiming for $> 10^3 - 10^4$ randomly-arranged clouds. Thus, the number of model clouds has to be small, the total optical depth of each cloud has to be limited, and/or the volume filling factors have to be rather large, of the order of $\Phi_V \sim 1$ (see also Dullemond & van Bemmelen 2005). Schartmann et al. (2008) showed that the SED of the nucleus of the Circinus galaxy as well as the position-angle- and baseline-dependence of the visibility is in good agreement with this kind of Monte Carlo models. Still, such direct Monte Carlo simulations take a lot of time and are, thus, not very flexible for modeling of observations.

As mentioned in Sect. 1, it is most likely that individual torus clouds are actually optically thick (see also Sect. 2.3). Based on optically thick clouds and the assumption of a low volume filling factor, $\Phi_V \ll 1$, Nenkova et al. (2002) used a probabilistic approach for cloud heating and obscuration, depending on several model parameters (see also Natta & Panagia 1984; Nenkova et al. 2008a). Nenkova et al. (2008b) presented model SEDs simulated via this approach which are in general agreement with observations. Beckert (2005) used a similar probabilistic model to reproduce the high-spatial resolution SED of NGC 1068. The benefit of this modeling approach is its time-efficient calculation of average model SEDs and average brightness distributions. On the other hand, as noted by Nenkova et al. (2008b), the probabilistic method is not capable of predicting variations in the overall SED and brightness distribution or the high-spatial frequency modulations of the interferometric visibilities and phases caused by the statistical distribution of dust clouds in the torus.

In Hönig et al. (2006) we presented a method to time-efficiently simulate torus model images and SEDs and account for the statistical nature of clumpy dust distributions. As for the probabilistic approach, our model strategy is based on separating the simulations of individual cloud SEDs and images, and the final SEDs and images of the torus. In a first step, the phase-angle-dependent emission for each cloud is simulated by Monte Carlo radiative transfer simulations. For that, we apply the non-iterative method delineated by Bjorkman & Wood (2001), based on work by Lucy (1999). In our previous model, we used the code *mcSim* (Ohnaka et al. 2006) which is able to simulate a variety of geometries. However, in order to obtain fast results for different dust compositions, we created a new Monte Carlo

code which is optimized for the AGN-cloud-configuration. For each given dust composition, we determine the sublimation radius $r_{\text{sub}} = r(T_{\text{sub}} = 1500 \text{ K})$ from the source, and simulate several clouds at different distances (normalized for r_{sub}). To finally simulate the torus emission, dust clouds are randomly distributed around an AGN according to some physical and geometrical parameters. Each cloud is associated with a pre-simulated model cloud, after accounting for the individual cloud's direct and indirect heating balance (see Sect. 2.6). The final torus image and SED is calculated via raytracing along the line-of-sight from each cloud to the observer. This method accounts for the full 3-dimensional geometry of the torus and involves statistical variations of randomly distributed clouds in a time-efficient way. We will characterize the model in more detail in the following sections.

2.2. AGN radiation

As AGN/accretion disk input spectrum, we use a four-component power-law which is approximately in agreement with the range of power-law fits to QSO composit spectra (e.g. Zheng et al. 1997; Manske et al. 1998; Vanden Berk et al. 2001; Scott et al. 2004):

$$F_{\nu} \propto \begin{cases} \nu^2 & \nu < 10^{14} \text{ Hz} \leftrightarrow > 3 \mu\text{m} \\ \nu^{1/3} & 10^{14} - 10^{15} \text{ Hz} \leftrightarrow 0.3 - 3 \mu\text{m} \\ \nu^{-1} & 10^{15} - 10^{16} \text{ Hz} \leftrightarrow 0.03 - 0.3 \mu\text{m} \\ \nu^{-2} & > 10^{16} \text{ Hz} \leftrightarrow < 0.03 \mu\text{m} (> 0.4 \text{ keV}) \end{cases} \quad (1)$$

The main difference to the spectrum used in Hönig et al. (2006) concerns the relatively blue part with $F_{\nu} \propto \nu^{1/3}$ in the optical to near-IR between 0.3 and $3 \mu\text{m}$. This spectral shape has recently been confirmed by near-IR polarimetry of quasars (Kishimoto et al. 2008).

We note that the actual shape of the spectrum is much less important for the heating of the dust than the total (spectrally-integrated) luminosity of the accretion disk, $L_{\text{bol}} = \int L_{\nu} d\nu$. In the optically-thick case, the totally absorbed heating power is $L_{\text{abs}} = \int Q_{\text{abs}}(\nu) L_{\nu} d\nu \sim 0.5 \times L_{\text{bol}}$, depending on the actual dust composition, where $Q_{\text{abs}}(\nu)$ is the absorption efficiency of the dust. Thus, the spectral shape of the incident radiation is integrated out in the process of radiative transfer.

2.3. Individual dust cloud properties and simulations

In the first step of our torus simulations, we calculate the emission profile of individual dust clouds. There are two main situations that have to be considered: (1) A dust cloud with external, non-isotropic heating by the AGN, and (2) a dust cloud with external, approximately isotropic heating by surrounding (directly-heated) clouds. For both situations, we use Monte Carlo simulations to calculate the dust radiative transfer in the clouds.

One fundamental property of the dust clouds in radiative transfer simulations is their optical thickness. If they are optically thin, i.e. $\tau_{\nu} \ll 1$, then they could be considered to have uniform temperature and the thermally re-emitted flux can be approximated by $F_{\nu} = \pi \tau_{\nu} B_{\nu}(T)$, where $B_{\nu}(T)$ is the Planck function at temperature T and τ_{ν} is the frequency-dependent optical depth. However, from observations of type 2 AGN, we know that both the dust and hydrogen columns are usually quite large, with the hydrogen column even Compton-thick. Associated torus dust temperatures are rather cool, peaking at $T \sim 200 - 300 \text{ K}$ (e.g. Jaffe et al. 2004; Tristram et al. 2007). Moreover, X-ray column density variability as seen in many AGN point to rather small

clouds and column densities of the order of 10^{23} cm^{-2} per cloud (e.g. Risaliti et al. 2007). To combine silicate absorption features as seen in type 2 AGN, Compton-thick obscuration, and small clouds, we infer that there are on average about 5–10 optically-thick clouds ($\tau_{\nu} \gg 1$) along a line-of-sight to the center in a type 2 AGN and that the volume filling factor of the torus $\Phi_V < 1$, i.e. the torus is clumpy. These cloud properties are, at least, qualitatively in agreement with models of self-gravitating dust and gas clouds in the shear of the gravitational potential of a super-massive black hole (Beckert & Duschl 2004; Hönig & Beckert 2007).

Since the exact dust distribution within a cloud is not known, we use a uniform density throughout the cloud, i.e. a density gradient $d\rho(r)/dr = 0$. While this might be oversimplified, we note that independent of the actual density distribution of an optically thick cloud, the bulk of the cloud re-emission originates from the optically-thin surface layer of the hot, directly-illuminated face of the cloud. Moreover, the gradient of the temperature at distance r from the cloud surface depends mostly on the total optical thickness at r and is supposedly very similar in all density distribution laws once the same optical depth is reached. So, the temperature of the non-illuminated side of the cloud is more or less independent of the dust density law within the cloud for the same optical depth through the diameter of the cloud (=“total optical depth” τ_V).

With the constant density law in our simulations, the cloud is subdivided into grid cells, where the dust density within each cell is optically thin. This guarantees that the steep temperature gradient in the surface layer on the hot face of the cloud is properly sampled.

For our cloud simulation, we use a spherical cloud geometry. In principle any kind of shape could have been chosen. However, the main difference between a sphere and, say, an ellipse is the different ratio of radial-to-perpendicular optical depth. As mentioned above, if the cloud has a total $\tau_V \gg 1$, then the dominant emission is coming from the optically-thin layer on the hot side of the cloud. Since the temperature in the layer is mostly independent of the density distribution in the rest of the cloud, the overall temperature of the hot cloud face is similar. For the cold face of the cloud, the main criterion is again the total optical depth within the cloud. For comparable total optical depths of two clouds with arbitrary shape¹, the cold-side temperatures are the same and, thus, the emerging emission. In summary, unless one insists on very peculiar cloud surfaces, the exact shape does not matter too much and a spherical cloud presumably catches the essence of the dust clouds in AGN tori.

For time-efficient simulations, we optimize the Monte Carlo code for the cloud-AGN-configuration. For that, we first determine the sublimation radius $r_{\text{sub}} = r(T_{\text{sub}})$ for a given dust chemistry and grain size composition, assuming a dust sublimation temperature $T_{\text{sub}} = 1500 \text{ K}$. Since r_{sub} scales with the AGN luminosity L as $r_{\text{sub}} \propto L^{1/2}$, the incident AGN flux on a dust cloud at r_{sub} is independent of the actual luminosity, $F_{\text{AGN}}(r_{\text{sub}}) \propto L/r_{\text{sub}}^2 = \text{constant}$. Thus, a single cloud database can be used for all AGN luminosities. Since the dust clouds are believed to be small, with a radius-to-distance-ratio $R_{\text{cl}}/r \lesssim 1$, we assume that the incident AGN radiation enters the model sphere on parallel rays. Moreover, the rotational symmetry of our clouds allows to reduce the model space for Monte Carlo simulations to a plane 3-dimensional grid with only 1 grid cell in

¹ The actual total τ_V 's that need to be compared depend on the exact shapes/elongations. Thus, one might see the total τ_V of the cloud in our model as some mean value representing all kind of shapes.

z -direction. These two modifications allow for a maximum number of photon packages to be simulated in a short time without suffering from strong Monte Carlo noise in the temperature of the individual grid cells. To be even less dependent on Monte Carlo noise, the final cloud SEDs and images are calculated via raytracing of the emission from each cell into the observer's direction (i.e. for different phase angles of the cloud): First, the full 3-dimensional temperature distribution is reconstructed from the 3D-plane temperature grid; then, the source function (thermal re-emission and scattering) for each cell is calculated and the path through the cloud is followed out of the cloud². In this way the angle-dependent source function of the cloud $S_{\nu}(\phi)$ is time-efficiently recovered.

The described fundamental simulation method is the same for both directly- and indirectly-heated clouds. The only difference occurs in handling the incident radiation field. Directly-heated clouds are irradiated by the accretion disk spectrum (see Sect. 2.2). The radiation enters the model sphere on parallel rays from one direction, and is then processed according to the Monte Carlo radiative transfer equations. One finally obtains the viewing-angle-dependent radiation field of direct heating, $S_{\nu;\text{DH}}(\phi)$. In contrast, the indirectly-heated clouds reside in the radiation field of surrounding clouds which is dominated by the emission of directly-heated clouds. We approximate this “diffuse radiation field” at distance r from the AGN by averaging the directly-heated cloud emission over all angles, $S_{\nu;\text{DRF}} = \int_0^{\pi} S_{\nu;\text{DH}}(\phi) \sin \phi d\phi$. Now, the photon packages of the diffuse radiation field $S_{\nu;\text{DRF}}$ enter the model sphere isotropically, and the rest of the radiative transfer simulation is the same as for directly-heated clouds. The result is the isotropic radiation field of indirect heating of a cloud $S_{\nu;\text{IH}}$.

In principle, this process of approximating the diffuse radiation in the torus is only the first step of an iteration scheme: Since the directly heated clouds are also indirectly heated, one has to include the diffuse radiation into their radiative transfer simulations. Then, a new diffuse radiation field has to be determined and the process be repeated. After several iteration steps, the final diffuse radiation field is obtained. The Monte Carlo method we used is quite flexible in implementing such a scheme without the need to reconsider direct illumination or previous steps (Krügel 2008, p.283): After the i -th simulation, a “corrected” diffuse radiation field has to be added which corresponds to the change with respect to the previous $(i - 1)$ -th iteration step, $dS_{\nu;\text{DRF}}^{(i)} = S_{\nu;\text{DRF}}^{(i)} - S_{\nu;\text{DRF}}^{(i-1)}$. However, it has been noted that the diffuse radiation field converges quite fast (e.g. Hönig et al. 2006; Nenkova et al. 2008a), so that one can consider $S_{\nu;\text{DRF}} \approx S_{\nu;\text{DRF}}^{(0)} = \int_0^{\pi} S_{\nu;\text{DH}}(\phi) \sin \phi d\phi$, as described in the previous paragraph, without the need of any further iteration. This makes simulations of cloud databases very fast and time efficient.

In summary, our simulations of dust clouds proceed as follows (see also Hönig et al. (2006); Nenkova et al. (2008a)): (1) 3D Monte Carlo simulations of directly AGN-heated clouds; (2) Approximation of the diffuse radiation field (i.e. heating of clouds not directly exposed to the AGN) by averaging the local emission of directly-heated clouds (see also Sect. 2.6 for a description of the assessment of the local circumstances within the torus); (3) 3D Monte Carlo simulation of clouds heated by the

² Note that this treatment limits the handling of scattering to single events. For our optically-thick clouds we tested this method against rigorous treatment of scattering with the *mcsim* code and found that any noticeable impact of the single-event-assumption is limited to wavelengths $\lesssim 1 \mu\text{m}$ and is of the order of 2%.

Table 1. Main physical properties of the dust compositions used in our study.

Name identifier	fractional composition		a_{\min} (μm)	a_{\max} (μm)	r_{sub}^a (pc)
	silicates	graphite			
standard ISM	0.53	0.47	0.025	0.25	1.1
ISM large grains	0.53	0.47	0.1	1.0	0.52
Gr-dominated	0.30	0.70	0.05	0.25	0.94

— Notes: ^a Sublimation radius r_{sub} at a dust temperature $T_{\text{sub}} = 1500 \text{ K}$ for $L_{\text{bol}} = 10^{46} \text{ erg/s}$. Sublimation radii for any other luminosity can be calculated by $r = r_{\text{sub}} \times (L_{\text{bol}}/10^{46} \text{ erg/s})^{1/2}$. L_{bol} is defined as $L_{\text{bol}} = \int L_{\nu} d\nu$ of the accretion disk. In our definition of the accretion disk spectrum, the reverberation radius from Kishimoto et al. (2007) for $L_{\text{bol}} = 10^{46} \text{ erg/s}$ would be $r_{\tau_K} = 0.38 \text{ pc}$, with approximately 25% scatter.

diffuse radiation field. This results in two cloud databases which are used for the torus simulations: one for directly-illuminated clouds and one for indirectly-heated clouds.

2.4. Dust properties and cloud emission

Previous torus studies used dust properties in line with standard grain sizes and chemical composition (e.g. Schartmann et al. 2005; Hönig et al. 2006; Nenkova et al. 2008b). In general, MNR distributions with a grain size power law distribution $\propto a^{-3.5}$ (a ... grain size) was assumed with lower and upper limits $a_{\min} \sim 0.005 - 0.01 \mu\text{m}$ and $a_{\max} \sim 0.25 \mu\text{m}$, respectively. The chemical compositions invoked 47% graphite and 53% silicates, either based on Draine & Lee (1984) or Ossenkopf et al. (1992) optical properties. Such dust compositions are considered as “standard ISM”. Recently it was suggested that the dust composition around AGN might be deviating from standard ISM. While Suganuma et al. (2006) confirmed the $L^{1/2}$ -dependence of the sublimation radius, the measured K -band reverberation radii of type 1 AGN are a factor of 3 smaller than what is expected from standard ISM dust. Kishimoto et al. (2007) suggest that this discrepancy might be caused by domination of larger grains, at least in the inner part of the tori.

We aim for simulating torus model SEDs and images for different physically-motivated dust compositions. In the first step, we analyze dust-composition effect on the individual dust clouds. The optical properties of the dust have been obtained using the *DUSTY* code (Ivezić et al. 1999). In the following, we present results for 3 different compositions:

2.4.1. Standard ISM

The starting point for our dust composition study will be the “standard ISM”. Physical dust properties are listed in Tab. 1. We show two versions of the standard ISM configuration: one uses Draine&Lee silicates, the other one consists of Ossenkopf silicates (see Sect. 2.4). The most important difference between both silicate types concerns the central wavelength and width of the silicate feature at around $10 \mu\text{m}$. For a given size distribution, the Draine&Lee silicate feature is much wider than the Ossenkopf feature. In Draine&Lee silicates, the central silicate feature wavelength is at $9.7 \mu\text{m}$ while the Ossenkopf silicate feature is centered at $10.0 \mu\text{m}$. The $10.0 \mu\text{m}$ central wavelength seems to be more consistent with peak silicate emission features of type 1 AGN as observed with *Spitzer*, while absorption features in type 2s usually have their center at $9.7 \mu\text{m}$ (e.g. Shi et al.

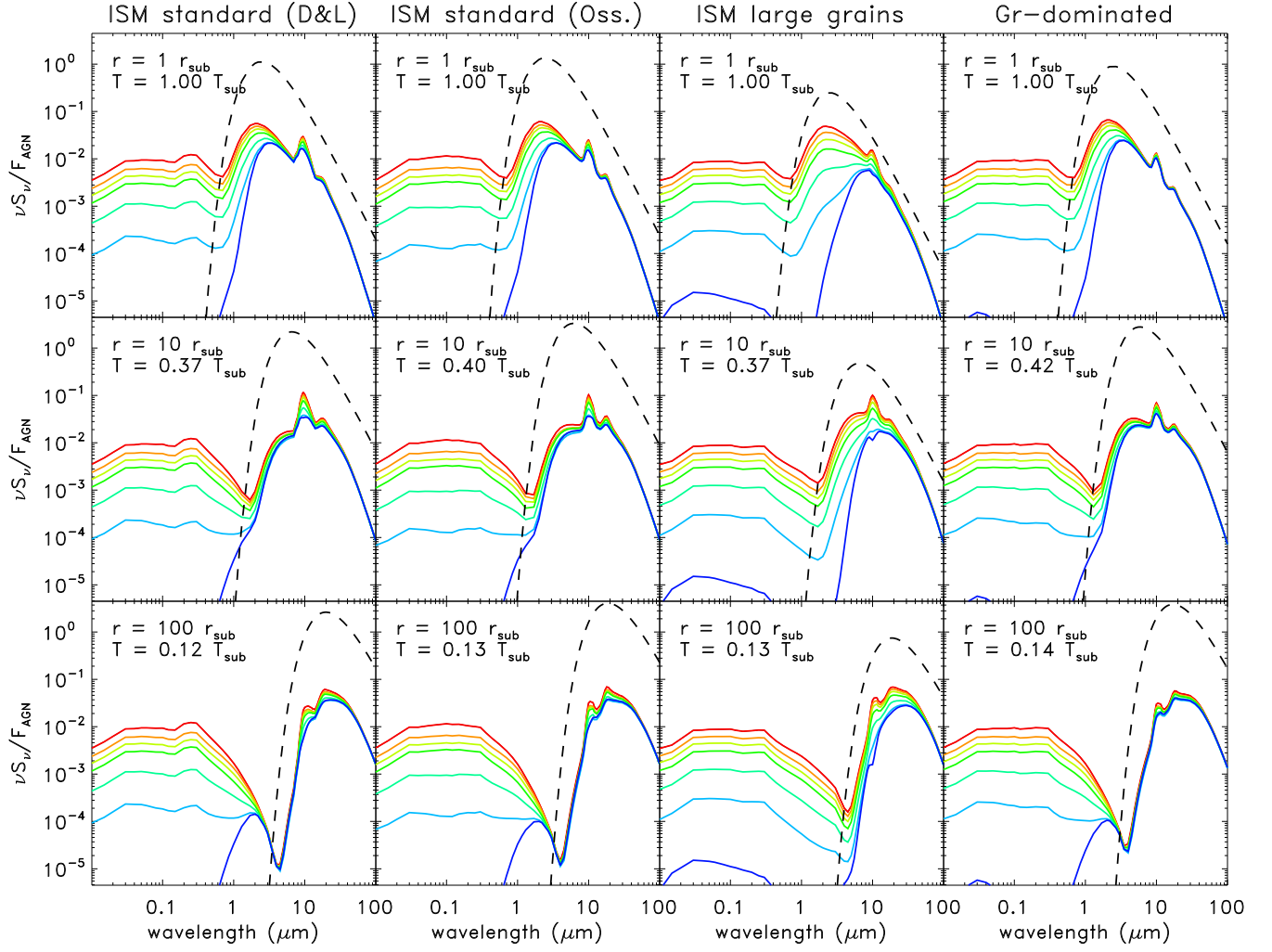


Fig. 1. Model source functions S_ν of directly AGN-heated clouds for several different dust configurations (from left to right column: ISM standard configuration with Draine & Lee silicates, Ossenkopf silicates, ISM large grains, and Graphite-dominated dust). Each row shows the emission of a cloud with $\tau_V = 50$ at the given AGN distance $r = r_{\text{sub}}$ (top), $10 r_{\text{sub}}$ (middle) and $100 r_{\text{sub}}$ (bottom), scaled to the total incoming flux of the AGN, $F_{\text{AGN}} = L_{\text{bol}}/(4\pi r^2)$. The corresponding hot-side temperature in units of $T_{\text{sub}} = 1500$ K are also given. The various lines represent a specific phase angle, ϕ , of the cloud in steps of 30° (red: $\phi = 0^\circ$, i.e. full hot side; purple: $\phi = 180^\circ$, i.e. full cold side). For comparison, we overplotted the corresponding black-body emission $B_\nu(T)$ with the same temperature as the hot side of the cloud at the same distance from the AGN (dashed line).

2006). We note, however, that radiative transfer effects can affect the exact shape of the feature.

Simulation results for directly-illuminated clouds with standard ISM dust configurations are shown in the two left columns of Fig. 1. We present clouds with a total optical depth $\tau_V = 50$ at three different distances $r = r_{\text{sub}}$, $10 \times r_{\text{sub}}$, and $100 \times r_{\text{sub}}$ from the AGN. Along with the distances, we also provide the maximum temperature of the hot side of the cloud in units of the sublimation temperature $T_{\text{sub}} = 1500$ K. The overplotted dashed lines show the black-body source function $B_\nu(T)$ with the same temperature as the hot side of the clouds at the same distance from the AGN. For both types of silicates, the temperature gradient on the directly-illuminated face is similar, with some trend of slightly higher temperatures for the Ossenkopf dust. The $r = 10 \times r_{\text{sub}}$ clouds serve best for illustration since the near-IR color is slightly redder for Draine&Lee silicates. The different temperature gradients are a result of slightly different absorption efficiencies – or more precisely: Planck mean opacities which, at the end, determine the temperature at a given radius in the ra-

diative transfer equations. The cloud emission is lower than the corresponding black-body emission by more than a magnitude indicating that ISM standard mixture clouds are not well represented by any black-body approximation. This is true for all dust compositions discussed here. It is worth noting that for the standard ISM configuration, the presented clouds with $\tau_V = 50$ are mostly optically thin in the infrared. This leads to only small differences in SED shapes for different phase angles ϕ^3 so that the hot-side emission shines all through the cloud and significantly contributes to the cold-side emission, e.g. as seen by the $9.7/10\mu\text{m}$ silicate emission feature in the $\phi = 180^\circ$ SEDs.

³ The phase angle ϕ is defined as the AGN-cloud-observer angle. $\phi = 0^\circ$ denotes the full visibility of the directly-illuminated face of the cloud (“full moon”), $\phi = 180^\circ$ describes the situation when only the cold side of the cloud is seen (“new moon”).

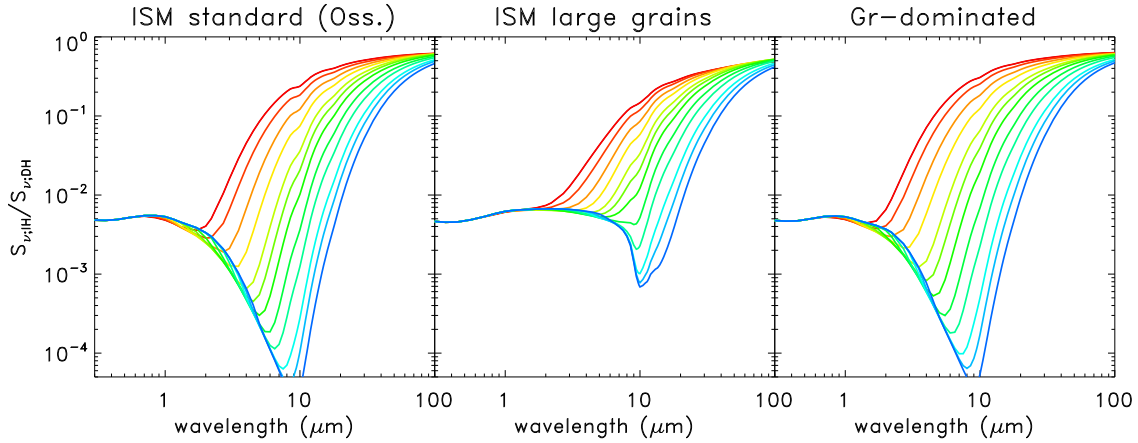


Fig. 2. Wavelength-dependent emission ratio between the source function of indirectly-heated clouds $S_{\nu, IH}$ and the hot face of directly-heated clouds $S_{\nu, DH}$. The various lines represent different distances r from the AGN with $r = 1, 1.5, 2.5, 4.7, 10, 15, 25, 40, 70, 100$ and $150 r_{\text{sub}}$ from top-red to bottom-blue. The left panel shows simulation results for “ISM standard” dust with Ossenkopf, the middle panel presents “ISM large grains”, and the right panels shows “Gr-dominated” dust.

2.4.2. ISM large grains

While near-IR reverberation mapping results of type 1 AGN confirmed the $L^{1/2}$ -dependence of r_{sub} , the observed K -band reverberation mapping radii r_{τ_K} are smaller by approximately a factor of 2–3 than what has been inferred from ISM dust (Suganuma et al. 2006; Kishimoto et al. 2007). Suggestions to solve this problem involve larger sizes of the dust grains than used in standard ISM distributions – at least in the innermost part of the torus which dominates the IR emission of type 1 AGN. To test this suggestion, we simulated dust clouds for a standard ISM composition with Ossenkopf silicates and limited the grain sizes to $0.1 - 1 \mu\text{m}$. This “ISM large grain” composition has a sublimation radius $r_{\text{sub}} = 0.52 \text{ pc} \times (L_{\text{bol}}/10^{46} \text{ erg/s})^{1/2}$ which is closer to the observed r_{τ_K} than the standard ISM dust (see Tab. 1).

The simulated dust cloud SEDs for the ISM large grain composition are shown in the third column of Fig. 1. The hot-side temperature gradient is comparable to clouds with ISM standard dust. The most notable difference concerns the change of the SED shape from $\phi = 0^\circ$ to 180° . While the previously-explored clouds show quite similar SEDs for all phase angles, the ISM large grain clouds become very red at near- and mid-IR wavebands for increasing ϕ . Moreover, the silicate feature at $10 \mu\text{m}$ turns from emission into absorption. The reason for this difference is the optical depth in the infrared: For both silicate and graphite, large grains have a much flatter extinction efficiency in the infrared. Thus, the cloud-internal extinction in the IR increases. While $\tau_{2.2 \mu\text{m}}/\tau_V \sim 0.05 - 0.06$ for the ISM standard configuration (depending on the silicate specy), the ISM large grains have $\tau_{2.2 \mu\text{m}}/\tau_V \sim 0.9$. In the silicate feature at $9.7/10 \mu\text{m}$, the ratios are $\tau_{\text{Si}}/\tau_V \sim 0.04$ and 0.1 , respectively. As a consequence, a cloud with $\tau_V = 50$ is also optically thick in the near- and mid-infrared. Thus, when seeing the cloud under large ϕ , the emission from the hot side of the cloud is blocked and the emerging SED is dominated by cool dust emission. This will also have an effect for the simulated torus SED since IR radiation can be efficiently absorbed which presumably leads to redder IR colors (see Sects. 3.2 & 3.4).

We note that the difference between black-body and hot-side cloud emission is smaller than for the other dust composition, as seen in Fig. 1. This implies that large dust grains are

better represented by a black-body approximation than smaller grains, although the difference is still almost an order of magnitude.

2.4.3. Graphite-dominated dust

In general, silicate dust grains have lower sublimation temperatures than graphite grains (e.g. Schartmann et al. 2005, for simulations with AGN radiation). This might result in a dearth of silicates in the torus, at least in the inner part. Moreover, since AGN are rather strong X-ray emission sources, it is doubtful that smallest dust grains can easily survive without being photo-destructed. For that, we modified the ISM composition by using only grains $> 0.05 \mu\text{m}$ and changing the chemical mixture to 70% graphite grains and 30% Ossenkopf silicates.

In the right-most column of Fig. 1, we show simulated cloud SEDs for this “Gr-dominated” dust. The overall SED shape resembles those of the standard ISM configurations. The dust is optically thin in the IR with $\tau_{2.2 \mu\text{m}}/\tau_V = 0.06$ and $\tau_{\text{Si}}/\tau_V = 0.02$. However, two important differences can be seen. First, the silicate emission feature at $10 \mu\text{m}$ is significantly reduced due to the reduction of silicate dust. This might be interesting given the relative weakness of silicate absorption and emission features observed in Seyfert galaxies (but see Sects. 3.2 & 3.4 for actual simulations). Second, the temperature gradient outward from r_{sub} is slightly flatter. As can be seen in the middle panel, the near-IR emission in the Gr-dominated dust clouds is bluer than for the standard ISM configurations and the ISM large grains. Therefore, it can be expected that for a given set of torus parameters (see Sect. 2.5), the radial emission size in the near- and mid-IR is slightly different than for the other dust compositions.

2.4.4. Indirectly-heated clouds

In Fig. 2, we illustrate the contribution of indirectly-heated clouds. The left panel shows the ratio of indirectly-heated cloud emission to directly heated emission as the ratio of the source functions $S_{\nu, IH}/S_{\nu, DH}(\phi = 180^\circ)$ for the ISM standard dust with Ossenkopf silicates at different distances r from the AGN. In the middle panel, we present results for the ISM large grain configuration, and in the right panel Gr-dominated dust was used.

Table 2. Cloud distribution functions and relations to physical parameters of the torus

Physical property	Function ^{1,2,3}
radial dust distribution	$\eta_r = \frac{1+a}{(R_{\text{out}}^{1+a}-1)} r^a \cdot \frac{1}{r_{\text{sub}}}$
vertical dust distribution	$\eta_z = \exp(-z^2/2H^2)$ or $\eta_\theta = \exp(-\theta^2/2\bar{\theta}_0^2)$
dust cloud radius	$R_{\text{cl}}(r) = R_{\text{cl};0} r^b \cdot r_{\text{sub}}$
total number of clouds	$N_{\text{tot}}^z = \sqrt{8\pi} N_0 h R_{\text{cl};0}^{-2} \frac{1+a}{3+a-2b} \frac{R_{\text{out}}^{3+a-2b-1}}{R_{\text{out}}^{1+a-1}}$ $N_{\text{tot}}^\theta = \sqrt{2\pi} N_0 f_{\theta_0} R_{\text{cl};0}^{-2} \frac{1+a}{3+a-2b} \frac{R_{\text{out}}^{3+a-2b-1}}{R_{\text{out}}^{1+a-1}}$ with $f_{\theta_0} = 2\bar{\theta}_0 \exp(-\bar{\theta}_0^2/2) \text{Erf} \frac{\pi-2i\bar{\theta}_0^2}{\sqrt{8}\bar{\theta}_0}$
volume filling factor at $z = 0$	$\Phi_{V;0} = \frac{4}{3} N_0 R_{\text{cl};0}^2 \frac{1+a}{R_{\text{out}}^{1+a-1}} \cdot r^{a+b}$

— Notes: ¹ r , z , H , and $R_{\text{cl};0}$ are given in units of r_{sub} ; ² Model parameters: (1) a : radial distribution power law index, (2) h : scale height, $h = H(r)/r = \text{const.}$ or half-opening angle θ_0 , (3) N_0 : mean number of clouds along equatorial line-of-sight, (4) $R_{\text{cl};0}$: cloud radius at r_{sub} (in units of r_{sub}), (5) b : cloud size distribution index, (6) R_{out} : the outer torus radius; ³ We define the altitudinal angle $\theta = 0$ in the torus mid-plane. Therefore we use, for convenience, the half-covering angle $\bar{\theta}_0 = \pi/2 - \theta_0$ instead of the half-opening angle θ_0 in the equations.

Except for the clouds closest to the AGN ($r \lesssim 5 \times r_{\text{sub}}$), the emission contribution of indirectly-heated clouds in the near- and mid-infrared below $10 \mu\text{m}$ is $\ll 0.1$ for the ISM standard and Gr-dominated dust. This means that indirectly-heated clouds are much cooler than the corresponding directly-heated cloud at the same r . This is slightly different for the ISM large grain configuration: Since these clouds are also optically thick in the infrared, they absorb the incident diffuse radiation field – which is dominated by IR photons – much more efficiently than the other two dust configurations. This results in better indirect heating so that the temperatures become higher.

Overall, it can be expected that the contribution of indirectly-heated clouds to the near- and mid-IR emission of the torus is quite small, so that the torus SED will be dominated by directly-heated clouds. This changes at longer wavelengths $> 10 \mu\text{m}$ where indirectly-heated clouds are almost as bright as their directly-heated counterparts. On the other hand, since the contributions of both types of clouds to the final torus SED is an interplay between cloud-cloud-obscuration and the fraction of illuminated clouds at r contributing to the diffuse radiation field, the actual cloud distribution in the torus has a strong influence.

2.5. Model parameters

The distribution of clouds in the torus is initially characterized by six model parameters. The torus parameters are (1) the radial dust-cloud distribution power-law index a , (2) the scale height h or the half-opening angle θ_0 , (3) the number of clouds along an equatorial line-of-sight N_0 , (4) the cloud radius at the sublimation radius $R_{\text{cl};0}$ in units of r_{sub} , (5) the cloud size distribution power-law index b , and (6) the outer torus radius R_{out} . From the model parameters, several other physical properties can be derived. However, we will show that some of these parameters can be considered only marginally influential on the torus SEDs and images, so that less parameters need to be constrained by observations. In the following, we will briefly show how the model parameter are associated with the dust distribution of the torus.

The most fundamental parameters deal with the geometrical distribution of the clouds in the torus. We separate the 3-dimensional dust distribution into a radial distribution power-law, $\eta_r \propto (r/r_{\text{sub}})^a$ and a vertical distribution $\eta_{z/\theta}$. For the vertical distribution, it has become common practice to use a Gaussian distribution. However, two different ways of defining this Gaussian have evolved from recent torus models. One possibility is to distribute the clouds perpendicular to the equatorial plane, i.e. in z -direction in a cylindrical coordinate system. The resulting distribution function $\eta_z \propto \exp(-z^2/2H^2)$ depends on the scale height $H(r) = h \cdot r$ at radial distance r . This implies that the torus flares with constant $H(r)/r$, as suggested by isothermal disks. Here, h is the fundamental parameter describing the vertical distribution. Another way of distributing clouds can be best understood in a spherical coordinate system: instead of defining the distribution function perpendicular to the equatorial plane, it is also possible to distribute the clouds along an altitudinal path, i.e. in spherical θ -direction with $\eta_\theta \propto \exp(-\theta^2/2\bar{\theta}_0^2)$. Here, $\bar{\theta}_0 = (\pi/2 - \theta_0)$ is the half-covering angle of the torus which is the complementary of the half-opening angle θ_0 (see remarks in Table 2). Which vertical distribution function to select depends on the idea how the vertical structure of the torus is formed. In Sect. 3.1 we discuss implication of using one or the other function and how they may be related to the torus dynamics. Table 2 shows the full distribution functions η_r , and $\eta_{z/\theta}$. The complete dust cloud distribution function

$$\eta(r, z/\theta) = 2\pi\eta_r \cdot \eta_{z/\theta} \quad (2)$$

is normalized so that $\int_1^{R_{\text{out}}} \eta_r dr = 1$ and $\eta_{z/\theta} = 1$ for $z = 0$ or $\theta = 0$. By this definition, η_r can be understood as the *normalized* number of clouds per unit length, so that

$$N_0\eta(r, z/\theta) = \pi R_{\text{cl}}^2 \rho_N \quad (3)$$

describes the (actual) number of clouds per unit length, where ρ_N denotes the cloud number density per unit volume. Note that r , z , H , and $R_{\text{cl};0}$ are given in units of r_{sub} .

After having fixed the distribution of clouds, the total obscuration (or dust mass) of the torus has to be defined. The most convenient way to do this is by defining the mean number of clouds N_0 that intersect the line-of-sight along a radial path in the equatorial plane. From N_0 it is easy to calculate the total number of clouds that have to be randomly distributed in the torus,

$$N_{\text{tot}} = N_0 \int \frac{\eta(r, z/\theta)}{\pi R_{\text{cl}}^2(r)} dV \quad (4)$$

which is essentially the integrated version of eq. (3) (see also Hönig et al. 2006; Nenkova et al. 2008a). Here, $R_{\text{cl}}(r) = R_{\text{cl};0} r_{\text{sub}} \cdot r^b$ denotes the radius of a dust clouds at radial coordinate r (in units of r_{sub}), with parameters $R_{\text{cl};0}$ and b as defined above. In Table 2, the explicit expression for N_{tot} is given for both vertical z - and θ -distributions.

Since we deal with a clumpy torus, it is most sensible to have a volume filling factor $\Phi_V < 1$ all over the torus. The volume filling factor Φ_V can be calculated by multiplying the cloud number density per unit volume ρ_N and the cloud volume $V_{\text{cl}} = 4/3\pi R_{\text{cl}}^3$, so that

$$\Phi_V = \frac{4}{3} N_0 \eta(r, z/\theta) R_{\text{cl}} \quad (5)$$

If restricting to the equatorial plane, the expression $\Phi_{V;0}(r) = \Phi_V(r, z \text{ or } \theta = 0)$ is derived as shown in Table 2.

We note that while consistency of our modeling approach requires $\Phi_V(r, z/\theta) < 1$ ($V(r, z)$ or (r, θ)), the torus brightness distribution and SED is not explicitly depending on Φ_V but rather on the combination of the individual parameters. Actually, approximately the same overall SEDs and images can be obtained when reducing Φ_V by reducing $R_{\text{cl};0}$, leaving all other parameters fixed (and calculate N_{tot} clouds according to the new $R_{\text{cl};0}$). This can be illustrated by introducing a simplified version of the clumpy torus model for type 1 AGN (see also Kishimoto et al. 2009). In a face-on view of the torus, the clouds are projected onto a ring ranging from r_{sub} to R_{out} . First, let us assume that most of the clouds are directly heated by the AGN. Then, a “surface filling factor” $\sigma_s(r)$ can be described as cloud number density ρ_N projected in z -direction⁴. If we consider η_z , the surface density becomes

$$\sigma_s(r) = \int_{-\infty}^{\infty} \pi R_{\text{cl}}^2 \cdot \rho_N \eta(r, z) dz = (2\pi)^{3/2} N_0 h \eta_r \cdot r_{\text{sub}} \quad (6)$$

with the explicit dependence $\sigma_s(r) \propto r^a$. In this definition, the surface density can be considered as a weighting factor of how much the clouds at radius r contribute to the total intensity. Here, N_0 and h are scaling constants which are not depending on the radial distribution. On the other hand, we can include a first-order approximation of obscuration effects, which accounts for a decreasing number of directly-illuminated clouds with radius, by multiplying $\sigma_s(r)$ with $\exp(-N(r, z))$ as described in the next Sect. 2.6. Finally, to obtain SEDs and brightness distributions in this simplified type-1 model, the luminosity $L_V^{(\text{tor})}$ is calculated by multiplying the surface filling factor with the source function of the clouds $S_V(r)$ and integrating from r_{sub} to R_{out} ,

$$L_V^{(\text{tor})} = 2\pi \int_1^{R_{\text{out}}} \sigma_s(r) \cdot S_V(r) r dr \quad (7)$$

Interestingly, $L_V^{(\text{tor})}$ does not depend on R_{cl} or b , so that it is difficult to constrain these parameters by observations. Instead, for the purpose of SED modeling, they should be selected in a way to fulfill the “clumpy criterium” $\Phi_V < 1$.

However, since R_{cl} and b control the total number of clouds N_{tot} , they have influence on small scale surface brightness variations resulting in slightly different SEDs for different random arrangements of clouds (see Hönig et al. 2006) or position-angle variations, which might be interesting for interferometry (see Sect. 3.5). Aside from $R_{\text{cl};0}$ and b , in Sect. 3.3 we will further show that R_{out} cannot be considered as a free parameter but has to be chosen in a sensible way depending on a .

In summary, the key model parameters which are directly accessible from observations are a , N_0 , and h or θ_0 .

2.6. Directly- and indirectly-heated clouds in the torus

After distributing the clouds in the torus, each clouds has to be associated with a corresponding cloud from the pre-calculated database. For that, a number of circumstances have to be considered. For given distance from the AGN and optical depth, the parameters which determine the temperature and emission of a cloud are (1) the fractional cloud area, f_{DH} , which is directly heated by the AGN, and (2) the fraction of directly-heated clouds in the cloud’s vicinity, $f_{\text{IH}}(r)$. f_{DH} determines the strength of direct heating. For $f_{\text{DH}} = 1$, the directly-heated re-emission of

⁴ Actually, $\sigma_s(r)$ can grow to larger than 1 which corresponds to the case that projection caused clouds to overlap. However, $\sigma_s(r) > 1$ is only valid if the dust column is optically thin at that wavelength.

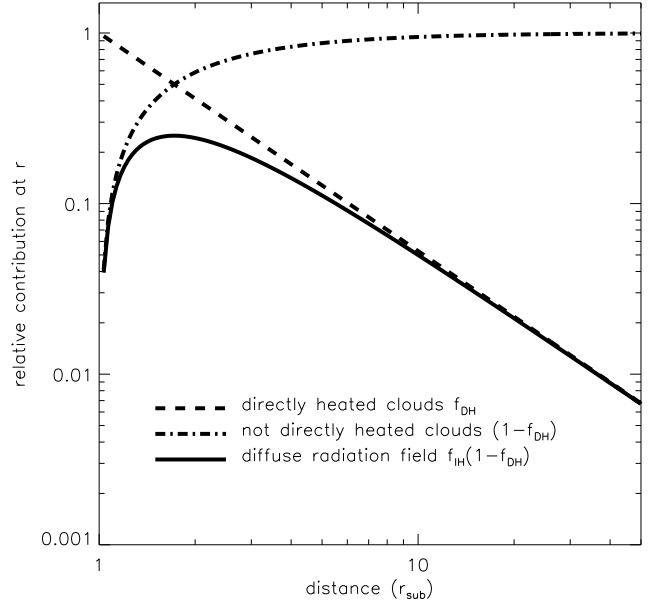


Fig. 3. Illustration of the contribution of directly- and indirectly-heated clouds. The dashed line represents the relative contribution of directly-heated clouds to the torus emission at given distance r from the AGN in the mid-plane, f_{DH} . The dashed lines shows the relative contribution $(1 - f_{\text{DH}})$ of indirectly-heated clouds at r if $f_{\text{IH}} = 1$. The solid line presents the actual contribution of indirectly-heated clouds due to the decreasing strength of the diffuse radiation field, $f_{\text{IH}}(1 - f_{\text{DH}})$.

the cloud is equal to the emission of the pre-calculated database cloud at the same distance $r_{\text{DB}} = r_{\text{cl}}$ from the AGN. If $f_{\text{DH}} < 1$, less direct energy is received and the cloud emission corresponds to a database cloud at distance $r_{\text{DB}} = r_{\text{cl}} / \sqrt{f_{\text{DH}}}$. The parameter $f_{\text{IH}}(r)$ determines the energy that is contained in the diffuse radiation field. It can be approximated by the probability $P_0(r, z)$ that a given cloud at r and z (or θ) is directly illuminated. Note that $P_0(r, z)$ can be considered a global, probabilistic version of f_{DH} , which is a local and individual property of each cloud. According to Natta & Panagia (1984), $P_0(r, z)$ can be derived from Poisson statistics as $P_0(r, z) = \exp(-N(r, z/\theta))$, where $N(r, z/\theta) = N_0 \int_0^s \eta(r, z/\theta) ds$ is the mean number of clouds along the path s from the center to $(r, z/\theta)$. In case $f_{\text{IH}} \equiv P_0(r, z) = 1$ (and $f_{\text{DH}} = 0$), the cloud’s contribution from indirect heating corresponds to the indirectly-heated database cloud emission at the same distance, $r_{\text{DB}} = r_{\text{cl}}$, otherwise $r_{\text{DB}} = r_{\text{cl}} / \sqrt{f_{\text{IH}}}$.

An interesting aspect is the actual contribution of indirectly-heated clouds to the overall torus emission. On one hand, with increasing r the fraction of clouds which are indirectly heated increase due to the increase in obscuration. On the other hand, the diffuse radiation field becomes weaker due to the absence of directly-heated clouds. In Fig. 3, we illustrate the relative contribution of directly- and indirectly-heated clouds to the torus emission at a given distance r in the torus mid-plane (i.e. $z = 0$ or $\theta = 0$). Here, we fix $N_0 = 5$, $a = -1.0$, and $R_{\text{out}} = 50^5$. The relative contribution, f_{DH} , of directly-heated clouds at distance r from the AGN is shown as a dashed line in Fig. 3. As a dashed-dotted line, we show the relative contribution of

⁵ For $a = -1.0$, the normalized radial distribution function becomes $\eta_r = (r \ln R_{\text{out}})^{-1}$.

indirectly-heated clouds if we assume that the vicinity of the indirectly-heated cloud is fully filled-up with directly-heated clouds to form the diffuse radiation field, i.e. $(1 - f_{\text{DH}})$. In reality, the number of directly-heated clouds around an indirectly-heated cloud decreases with r , as outlined in the previous paragraph. The solid line illustrates this effect. It shows the contribution of indirectly-heated clouds at distance r , considering the decrease of directly-heated clouds in the vicinity, $f_{\text{IH}}(1 - f_{\text{DH}})$. As can be expected from energy conservation, this line is lower than the directly-heated cloud contribution and approaches it asymptotically with increasing r . Given their general higher temperatures, this illustrates that directly-heated clouds dominate the torus emission over indirectly-heated clouds – at least in more or less face-on geometries where line-of-sight obscuration effects play a minor role.

3. Modeling results and discussion

In the following, we will address several topics related to understanding, modeling and interpreting IR observational data of AGN. Instead of presenting a full model grid analysis of all model parameters, we concentrate on those identified as being crucial (a , N_0) and discuss issues that have not yet been explored in literature (vertical distribution, dust composition, R_{out} selection). For a more general investigation of model parameters of clumpy tori, we refer to the recent literature (Hönig et al. 2006; Schartmann et al. 2008; Nenkova et al. 2008b).

3.1. Different vertical distribution functions

In Sect. 2.5, we introduced two different ways of distributing the clouds vertically with distribution functions η_z and η_θ . While, at first glance, the difference might be technical, simulations show significant impact on the selection of the distribution function. Fig. 4 presents torus model SEDs for a set of parameters and for clouds distributed according to η_θ (solid lines) and η_z (dashed lines) at inclination angles $i = 0^\circ$ (face-on; red), 45° (green), and 90° (edge-on; blue). For this illustration, we used a radial power-law index $a = -1.0$, the mean number of clouds along an equatorial line-of-sight $N_0 = 7.5$, an outer radius $R_{\text{out}} = 50$, and, as throughout the paper, a half-opening angle $\theta_0 = 45^\circ$. As can be seen, the η_θ (“spherical”) distribution shows a narrower variation with inclination angle of the overall SED than the η_z (“cylindrical”) distribution. Particular differences are notable in the silicate feature as well as in the near-IR where the spherical distribution is redder.

The reason for these differences originate in the obscuration properties. Let us consider a pole-on view onto the torus. In the cylindrical case, the cloud radii at the projected distance r_{proj} from the AGN are given by $R_{\text{cl}}(r_{\text{proj}}) = R_{\text{cl}}(r)$ for $r_{\text{proj}} = r$, independent of z . In the spherical case, the clouds are distributed along circular arcs and the cloud radius at r_{proj} depends on the “origin” location, so that $R_{\text{cl}}(r_{\text{proj}}) \geq R_{\text{cl}}(r)$ for $r_{\text{proj}} = r$. The higher the position of the cloud above the mid-plane, the larger the radius. Thus, the hot emission from the inner part of the torus can in part be obscured by large clouds at high elevation above the torus mid-plane. In edge-on cases, this results in more efficient obscuration of clouds which are at small r from the nucleus but at some height over the mid-plane.

The difference can also be noted in the images. Fig. 5 shows a comparison between model images and visibilities of the cylindrical and spherical distributions at $i = 0^\circ$ and 90° . In the face-on geometry, the effect of obscuration by clouds at some elevation above the mid-plane can be seen: these clouds produce apparent

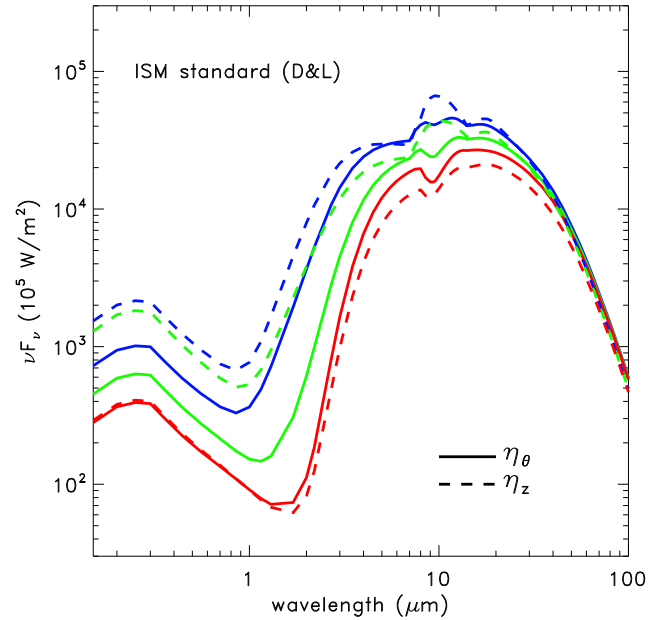


Fig. 4. Comparison of model SEDs for two different ways of distributing the clouds vertically. The solid lines show model SEDs for a clumpy torus where the clouds have been distributed according to η_θ , while the dashed lines represent model SED for the η_z function. Red, green, and blue indicate inclination angles 0° , 45° , and 90° , respectively.

“holes” in the otherwise disk torus image. This effect, however, is not reflected in the face-on visibilities (red lines) which show a similar scatter for both distribution functions. In the edge-on case, the larger obscuration in the spherical distribution causes a smear-out of the “boxy” or “disky” geometry seen for η_z , leading to a more circular aspect. This is also represented in the edge-on visibilities (blue lines). The spherical distribution has quite similar baseline-dependent visibilities for different position angles, while the disk structure in the cylindrical distribution causes a notable change for different position angles. For these illustrations, we used the standard ISM dust compositions and note that the described effects are the same for the other dust compositions.

What does the choice of the vertical distribution function mean physically? Two prominent competing ideas for the vertical extension of the torus are the accretion (e.g. Krolik & Begelman 1988; Vollmer et al. 2004; Beckert & Duschl 2004) and the disk-wind scenarios (Königl & Kartje 1994). In the case of accretion, it is assumed that the gas and dust clouds are accreted from galactic scales. Occasional scattering among these clouds causes some clouds to lift-off from the torus mid-plane. If the accretion rate is sufficient, each cloud undergoes approximately one scattering event per orbit and the torus becomes geometrically thick. In the disk-wind scenario, the geometrical thickness of the torus is caused by a clumpy wind from the central torus plane. Here, radiation and/or hydrodynamic pressure lead to an uplift of dust, and the mass support for optical thickness is also controlled by accretion. In any case, the fundamental picture for a clumpy torus breaks down to accretion and an uplifting mechanism, let it be dynamical or radiation pressure, and leads to similar demands on the physical environments (Elitzur & Shlosman 2006; Hönig & Beckert 2007): it is required that the local

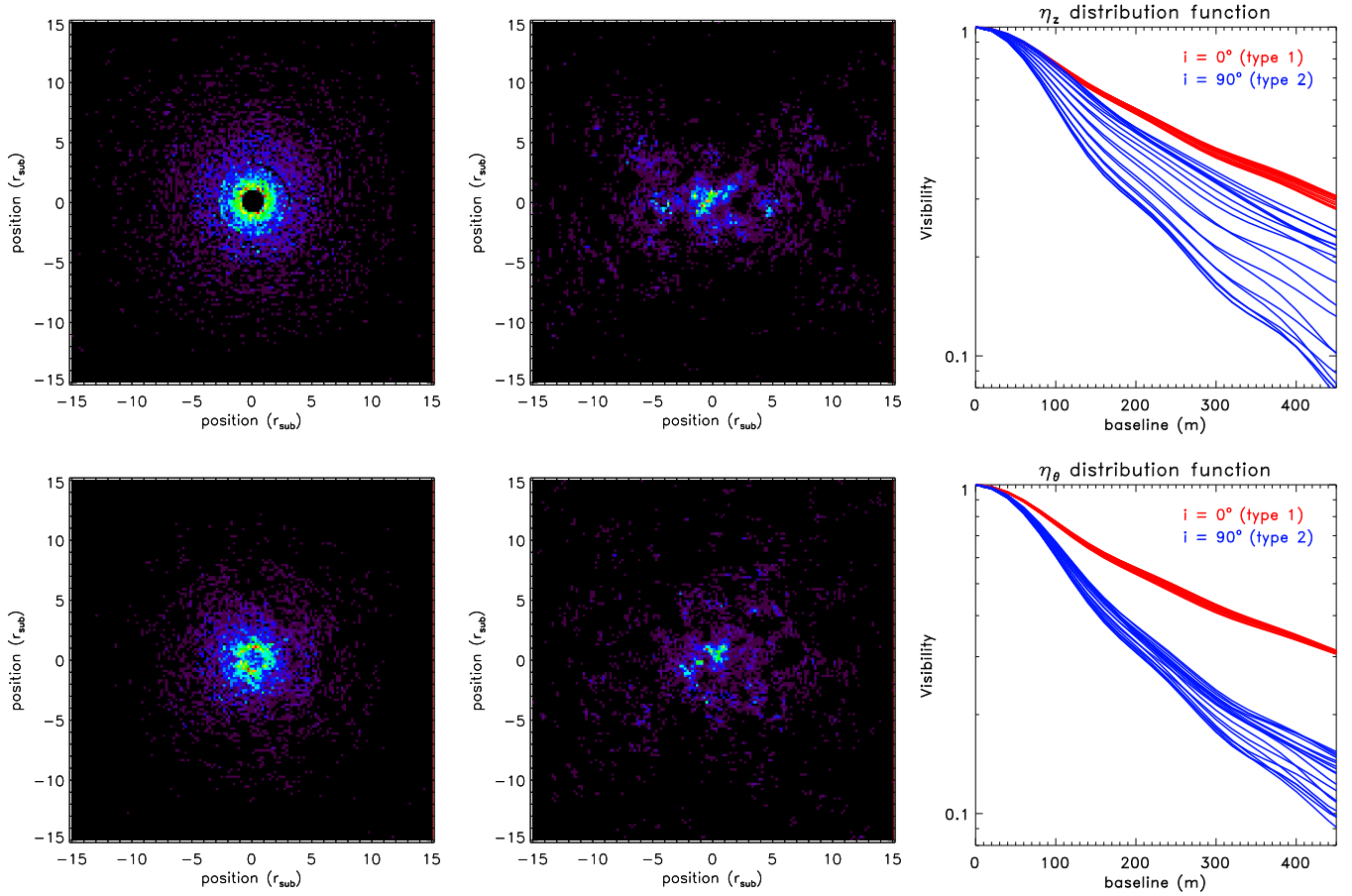


Fig. 5. Comparison of model images (left panels: face-on; middle panels: edge-on) and $8\ \mu\text{m}$ baseline-dependent visibilities (right panels) for the two different vertical distribution functions. For the visibilities, the AGN is assumed to reside at a distance of 15 Mpc with a sublimation radius $r_{\text{sub}} = 0.025\ \text{pc}$. For both face-on (red lines) and edge-on (blue lines) geometry, visibilities for position angles from 0° to 180° are shown in steps of 18° . *Top:* Cylindrical distribution function η_z ; *Bottom:* Spherical distribution function η_θ . The images are crops of the inner $30\ r_{\text{sub}}$.

random motion is of the same order as the local ordered motion (\approx Keplerian velocity). In this case the interplay of uplift and gravitational pull will force the cloud on a curved path in vertical direction, approximately preserving the distance from the AGN. The corresponding vertical cloud distribution can probably be best represented by the η_θ function. The η_z distribution would represent the case where the uplift speed is much higher than the ordered motion (\approx escape velocity). In reality, some clouds will receive strong uplift accelerations while others will experience only moderate uplift. Since we expect that the typical case will be the moderate uplift, the η_θ distribution function will be used in the rest of the paper.

3.2. The radial dust distribution and its influence on type 1 AGN data

Type 1 AGN are interesting cases for physical interpretation of observations since obscuration effects do not play a major role in the torus emission (see Sect. 2.6). In the simplified type 1 model presented in Sect. 2.5, the observed torus SED $L_\nu^{(\text{tor})}$ can be approximated by an integration over all radii (from r_{sub} to R_{out}) of the cloud source function $S_\nu(r)$ times the surface filling factor $\sigma_s \propto N_0 \cdot r^a$. As illustrated in Sect. 2.4, the cloud source function is depending on the r -dependent temperature $T(r)$ and the dust absorption efficiency. In the blackbody limit, the source function

is equal to the Planck function $B_\nu(T)$. Although in “real” tori obscuration effects *will* play a role even in type 1 AGN, such effects are smoothed since clouds above the torus mid-plane will fill-up some of obscuration “holes”. Thus, for a given dust composition, type 1 SEDs are mostly sensitive to the radial distribution of the dust clouds (here, the radial power law index a) and the number of clouds along an equatorial line-of-sight N_0 , and can possibly be used to constrain these parameters. Such simplification should capture the overall essence of the torus SEDs and spatial information as obtained by interferometry (see Kishimoto et al. 2009), although details, such as the silicate feature, may not be properly reproduced. We leave it up to future work to compare the outlined simplification to the more sophisticated 3D torus model which is used in this paper. However, in both pictures, observing $L_\nu^{(\text{tor})}$ allows for constraining a and N_0 for given cloud source functions $S_\nu(r)$.

In Fig. 6, we present comparison of model SEDs for different radial power-law indices a , being influenced by the dust composition and the mean number of clouds in the equatorial line-of-sight N_0 . The models SEDs are scaled to a distance corresponding to the sublimation radius r_{sub} . In that way, the model SEDs are independent on assumptions of the bolometric luminosity but can be used to constrain the sublimation radius from

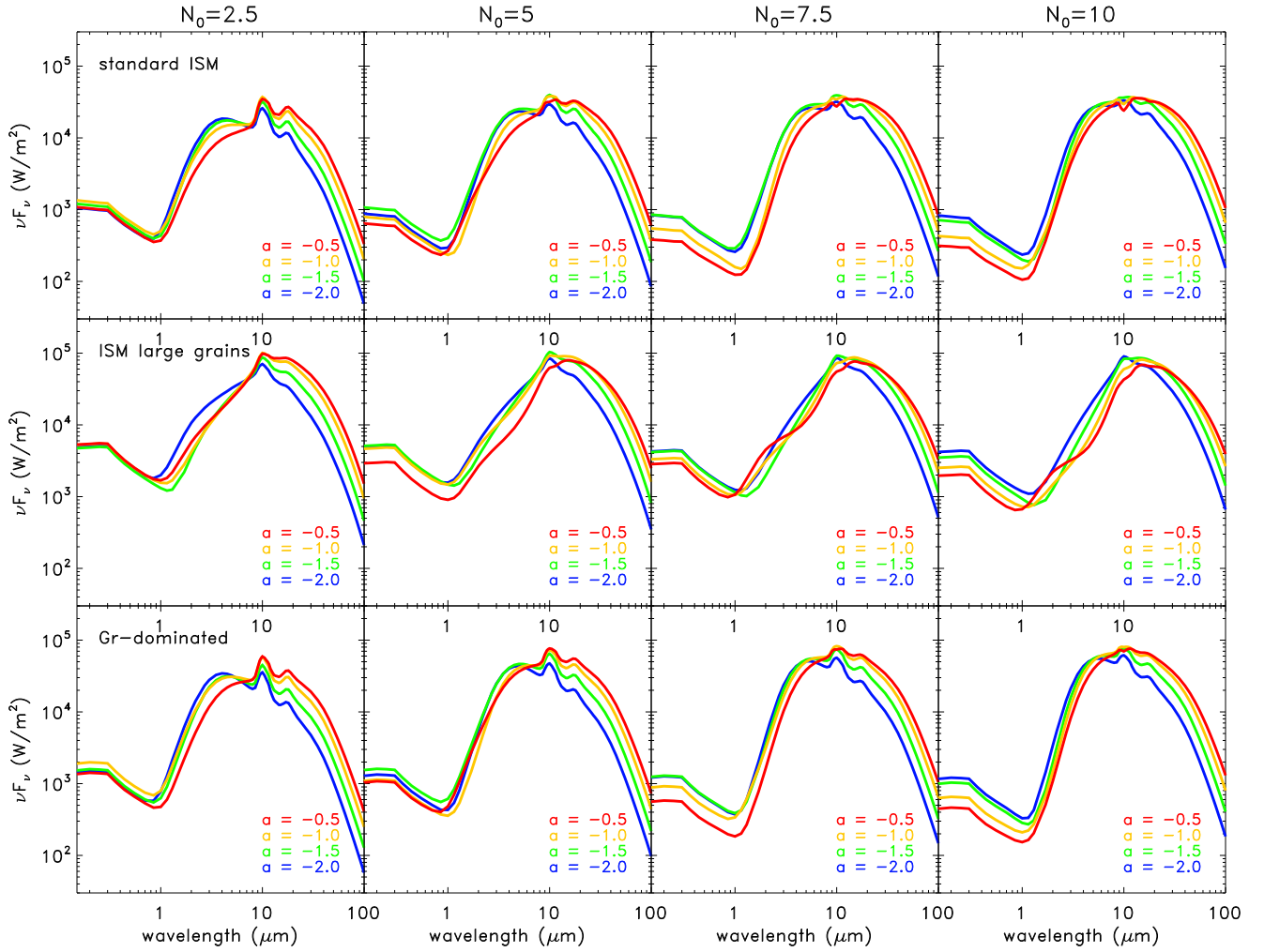


Fig. 6. Model SEDs of type-1 AGN (inclination angle $i = 15^\circ$) for different dust compositions, mean number of clouds in equatorial line-of-sight N_0 , and radial power law indices a . The top row show model models with the standard ISM composition, the middle row is for large grains, and the bottom row represents GR-dominated dust. From left to right, the columns show an increasing mean number of clouds in the equatorial line-of-sight, $N_0 = 2.5, 5, 7.5,$ and 10 , respectively. In each panel, we plot SEDs of a representative random cloud distribution for radial power law indices $a = -0.5$ (red), -1.0 (yellow), -1.5 (green), and -2.0 (blue).

IR observations. Observed fluxes νf_ν can be easily compared to model fluxes νF_ν via the relation

$$\nu F_\nu = \nu f_\nu \cdot \left(\frac{D_L}{r_{\text{sub}}} \right)^2 \quad (8)$$

where D_L is the distance to the AGN and r_{sub} is the sublimation or reverberation radius. For the presented models in Fig. 6, we fix $R_{\text{out}} = 50$ and, as for the rest of the paper, $R_{\text{cl},0} = 0.035$ and $b = 1.0$ (see Sect. 2.5). The top row shows models with the standard Ossenkopf ISM composition, the middle row is for large grains, and the bottom row represents Gr-dominated dust. From left to right, the columns show increasing $N_0 = 2.5, 5, 7.5,$ and 10 , respectively. In each panel, model SEDs for $a = -0.5, -1.0, -1.5,$ and -2.0 are shown.

All models have in common that the total SED becomes redder when the power-law becomes flatter, simply because cooler dust at larger distances is involved with the flat power-law distributions. The standard ISM and Gr-dominated dust distributions show similar overall SEDs and similar trends when changing N_0 or a . For small N_0 , the silicate emission features are strongly

pronounced, and there is quite some difference in the continuum shape for different a . While the flat distributions ($a = -0.5$ and -1.0) peak in the continuum at long mid-IR wavelengths, the steeper distributions ($a = -1.5$ and -2.0) have their continuum emission peak in the near-IR, which is caused by the fact that in the latter case most of the dust is confined to small distances from the AGN, i.e. the average dust temperature is rather high. With increasing N_0 , the silicate emission features become shallower and can even turn into absorption ($N_0 = 10, a = -0.5$, standard ISM). Moreover, the red continuum in flat distributions becomes bluer and the blue, steep dust distribution become redder, so that the difference in SED for varying a is generally reduced. This is caused by obscuration effects within the torus: if N_0 increases, clouds at larger distances contribute less to the overall emission since there is less chance that they are directly exposed to AGN emission. That effect is strongest for the flat distributions. In addition, the denser packing of clouds for larger N_0 results in torus-internal obscuration which reduces the silicate emission feature and makes the near-IR part of steep power-law indices redder. The main difference between Gr-dominated and ISM standard dust is the overall color. Since Gr-dominated

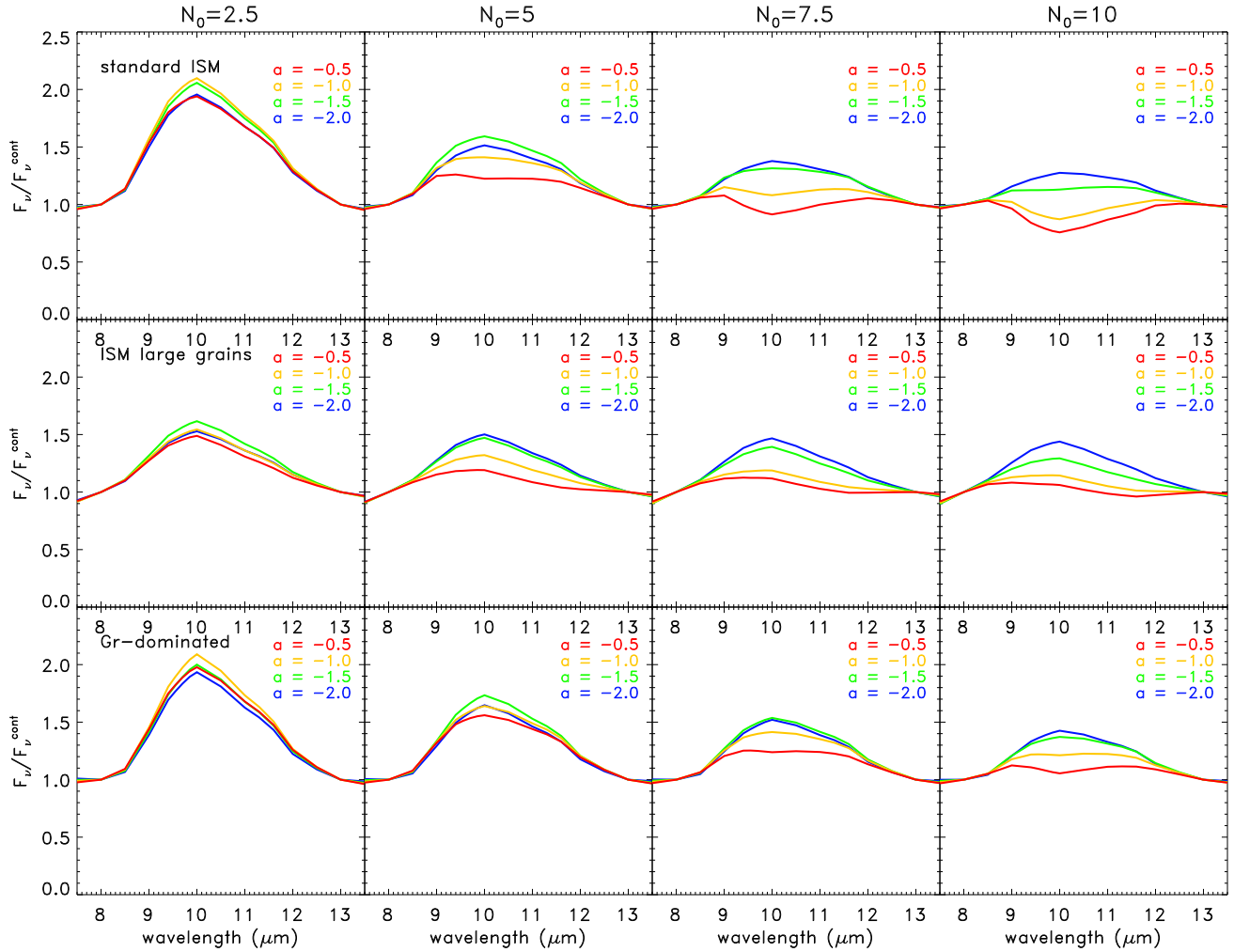


Fig. 7. Continuum-normalized $10\mu\text{m}$ model silicate features in type-1 AGN (inclination angle $i = 15^\circ$) for different dust compositions, mean number of clouds in equatorial line-of-sight N_0 and radial power-law indices a . The top row show model models with the standard ISM composition, the middle row is for large grains, and the bottom row represents Gr-dominated dust. From left to right, the columns show an increasing mean number of clouds in the equatorial line-of-sight, $N_0 = 2.5, 5, 7.5,$ and 10 , respectively. In each panel, we plot SEDs of a representative random cloud distribution for radial power law indices $a = -0.5$ (red), -1.0 (yellow), -1.5 (green), and -2.0 (blue).

dust has a slightly flatter temperature law (see Sect. 2.4.3), the torus SEDs are slightly bluer than for the ISM standard dust. It can also be noticed that, for a given set of parameters, the total flux level of Gr-dominated SEDs is approximately a factor of 2 higher than for the ISM standard SEDs.

The ISM large grain dust shows completely different SEDs. No matter which a or N_0 is selected, the peak continuum emission is always located at wavelengths $> 10\mu\text{m}$ in νF_ν . The silicate emission features are hidden under the very red slope which is present even in the mid-IR. The $2\mu\text{m}$ -to- $10\mu\text{m}$ νF_ν ratio is $\gtrsim 10$, while in the other dust configurations it is $\lesssim 3$. The reason for this behaviour is the dust-specific τ in the infrared (see Sect. 2.4.2). For the clouds with total $\tau_V = 50$, the large grains are optically thick in the near- and mid-IR. Thus, cloud-internal obscuration as well as torus-internal obscuration in vertical direction reduce the near- and mid-IR flux. For increasing N_0 , the SEDs become even redder, due to the same effects as described in the previous paragraph.

In the $N_0 = 7.5$ and 10 cases of the ISM large grain dust, the SEDs in the near-infrared get slightly “disordered” where differ-

ent a SED lines cross each other and show some wiggling. This is a statistical effect specific to the selected random arrangement of clouds. As we pointed out in Hönl et al. (2006), for a given set of model parameters, the different realizations of the random cloud arrangement show slight differences in the resulting SED and visibilities. The degree of variation among the different random cloud arrangements depends on the optical depth at the given wavelength. If the optical depth of the cloud $\tau_\lambda < 1$, almost no variations are expected. On the other hand, if $\tau_\lambda > 1$, then variations become significant. Thus, such variations are usually restricted to more or less edge-on geometries where obscuration plays a major role. However, in the case of the ISM large grain dust, the high τ_λ in the infrared make obscuration effects substantial also at wavelengths $> 1\mu\text{m}$, even in type 1 AGN if N_0 is large enough.

Overall, for a given dust composition, the differences in the near-IR colors for varying a and/or N_0 are not very dramatic leading to model parameter degeneracies between a and N_0 when modeling IR photometry data. To better constrain physical parameters or parameter tendencies, other observables

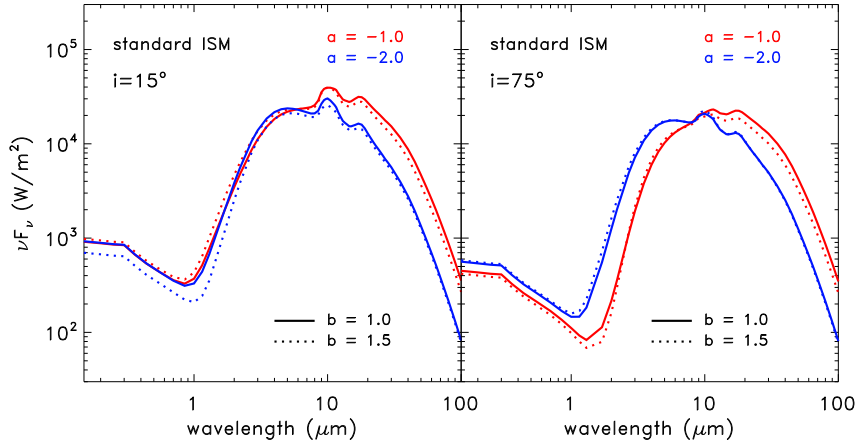


Fig. 8. Comparison of model SEDs for different cloud radius power-law indices $b = 1.0$ (solid lines) and 1.5 (dotted lines). In each panel we compare b for different radial power-law indices $a = -1.0$ (red lines) and -2.0 (blue lines), with fixed $R_{\text{out}} = 50$ and $N_0 = 5$ for the standard ISM dust. The left panel shows a type-1 SED ($i = 15^\circ$), and the right panel shows a type-2 SED ($i = 75^\circ$).

have to be taken into account. One possibility is a comparison of the observed $10\mu\text{m}$ silicate features with models which show a variety of strengths for different model parameters (e.g. Hönig et al. 2006; Schartmann et al. 2008; Nenkova et al. 2008b, or Indebetouw et al. (2006) in the case of YSOs). We note that, in principle, the $18\mu\text{m}$ feature might also be used. On the other hand, the lack of high-spatial resolution data in this wavelength range make it difficult to judge from which spatial scales the emission is originating. Therefore, we concentrate on the $10\mu\text{m}$ feature for which ground-based sub-arcsecond data is available. In Fig. 7, we show the $10\mu\text{m}$ silicate features for different model parameters. To isolate the features, a linear fit to 8 and $13\mu\text{m}$ continuum has been made and the model SEDs have been normalized by the continuum. While this is a quite simplified method, isolating the $10\mu\text{m}$ silicate feature is to some extent always depending on the used method since it merges into the $18\mu\text{m}$ feature towards longer wavelengths and the continuum changes its shape in the same wavelengths region due to radiative transfer effects. Nevertheless, such methods provide an easy tool to illustrate the strength of the silicate feature. As in the previous figures, we present increasing N_0 from 2.5 to 10 in the columns from left to right. In each column, we color-coded the individual a -indices from -0.5 to -2.0 as in Fig. 6. From top to bottom, the rows show standard ISM, large grain, and Gr-dominated dust compositions. We will not attempt to analyze the exact shape of each set of model parameters in detail, but would like to describe the overall behavior. The silicate features in the type-1 orientation are seen in emission for most parameters, as expected and already noted above. However, with increasing N_0 and/or flatter radial dust distribution ($a = -0.5$ to -1.0), the features become weaker and can even turn into absorption. This is due to the interaction of obscuration in vertical direction (for larger N_0 , more clouds are present in vertical direction) and cloud distribution (flatter distributions are dominated by cooler dust emission). In general, the ISM standard configuration shows weaker emission features than the other dust configurations. Actually, the Gr-dominated dust clouds have a lower τ_{Si}/τ_V ratio and ISM large grain clouds have a higher τ_{Si}/τ_V ratio than the ISM standard grains. Thus, by studying the different chemical compositions, we also see the effect of different cloud optical depths. In conclusion, the appearance of the silicate feature in type 1 AGN is mainly depending on the selection of a , N_0 , and the cloud optical depth in the silicate feature which is related to τ_V and the dust composition.

It is worth mentioning that variations in R_{cl} or b do not have a major impact on the overall SED shape, just as expected (see Sect. 2.5). As an illustration we present SEDs for $b = 1.0$ (solid lines) and 1.5 (dotted lines) and $a = -1.0$ (red lines) and -2.0 (blue lines) in Fig. 8, with fixed $R_{\text{out}} = 50$ and $N_0 = 5$ for the standard ISM dust. The left panel shows a type-1 SED ($i = 15^\circ$), and the right panel shows a type-2 SED ($i = 75^\circ$). For both a values shown, the solid and dotted lines, representing the different b -values, are very similar. This might be surprising since one would have naively thought that if the cloud surface is larger at greater distances from the AGN, there should be much more cold emission from these distances contributing to the SED, making it quite red. However, this effect is cancelled out by the fact that with growing cloud radius/surface, torus-internal radial obscuration also becomes larger. Thus, it is less likely that a cloud at large distance from the AGN is directly illuminated which effectively reduces the diffuse radiation that indirectly heats the clouds. In fact, the parametrization of η_r is chosen so that the cloud size does not matter much (see Sect. 2.5). On the other hand, we noticed during our parameter studies that variations for different random cloud arrangements increase with cloud radius, i.e. with R_{cl} and b . This is an effect of statistics: If $R_{\text{cl}}(r)$ is large at any r , only few clouds are distributed in the torus so that variations become strong. If $R_{\text{cl}}(r)$ is small, the torus consists of more clouds so that the overall appearance is smoothed and variations become less. In conclusion, b and R_{cl} cannot be constrained by SED modeling since they have at best a minor impact on the SED, but they might influence the interpretation of IR interferometry data, e.g. by showing distinct variations of visibility scans over position angle for a fixed baseline, or as discernible signals in the phase information.

We summarize that type 1 SEDs can be used to constrain the radial distribution index, a , of dust clouds in the torus and the mean number of clouds along an equatorial line-of-sight N_0 .

3.3. The outer radius of the torus – a real model parameter?

When modeling the IR SEDs, there is often a question arising: How far outward does the torus extend in the model? Since our model defines R_{out} as a parameter, one might think that the R_{out} value would be the correct answer. However, it is not all that simple. Due to the decrease of cloud temperature with distance and the corresponding decrease of total intensity, clouds at different distances from the AGN contribute different fractions to

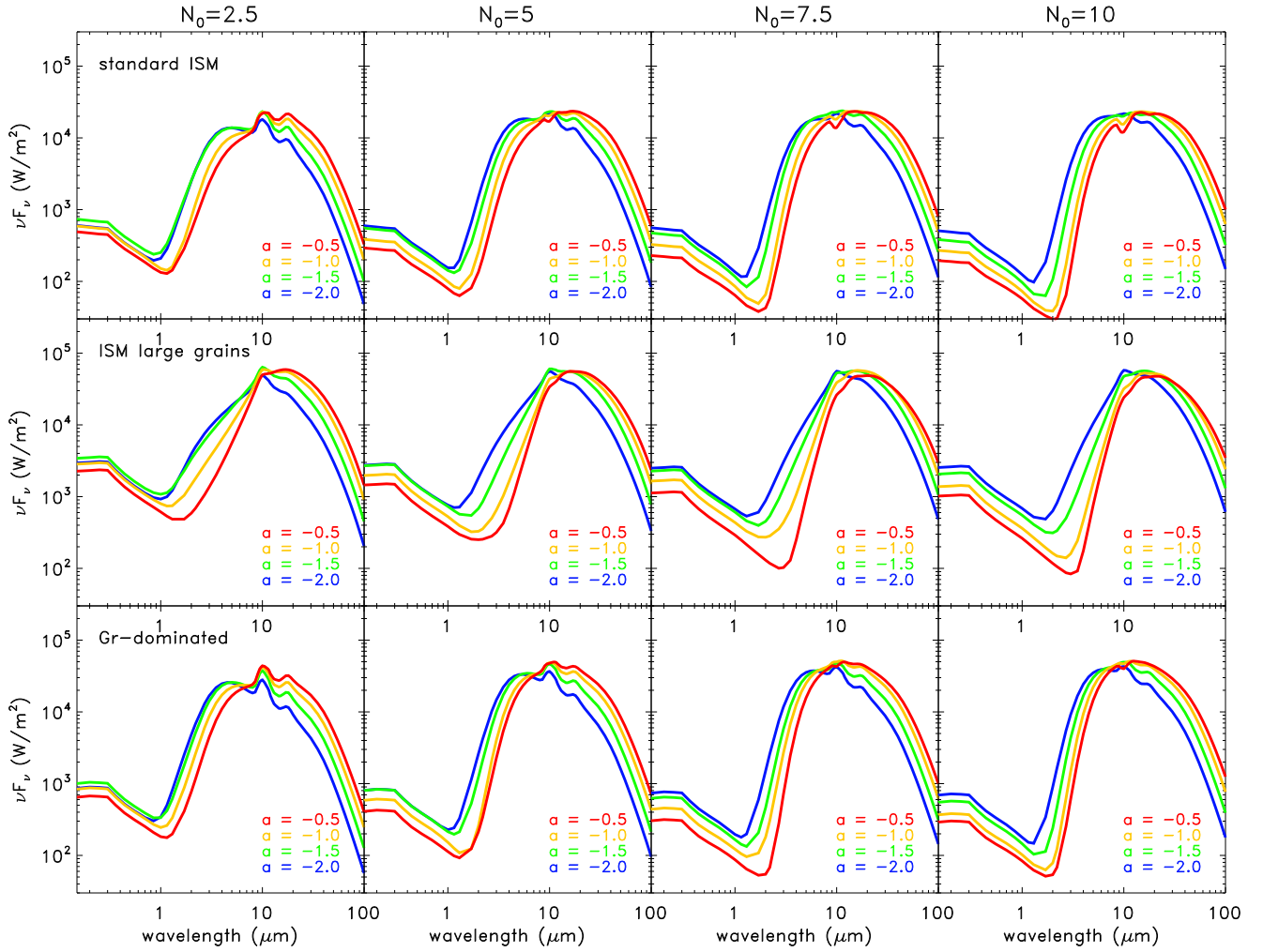


Fig. 9. Model SEDs of type-2 AGN (inclination angle $i = 90^\circ$) for different dust compositions, mean number of clouds in equatorial line-of-sight N_0 , and radial power law indices a . The top row show model models with the standard ISM composition, the middle row is for large grains, and the bottom row represents GR-dominated dust. From left to right, the columns show an increasing mean number of clouds in the equatorial line-of-sight, $N_0 = 2.5, 5, 7.5,$ and 10 , respectively. In each panel, we plot SEDs of a representative random cloud distribution for radial power law indices $a = -0.5$ (red), -1.0 (yellow), -1.5 (green), and -2.0 (blue).

the total torus flux at a given wavelength. In general, clouds at the innermost torus region contribute most of the near-IR light while clouds at larger radii are the dominant source of the mid-IR emission. As described in the previous section, this distance-dependence of the cloud source function is convolved with the cloud surface filling factor $\sigma_s(r)$ in the final torus SED. Thus, the actual size of the emission region is depending on the observed wavelength λ , the radial dust distribution $\propto r^a$, and to less degree the number of clouds along the equatorial line-of-sight N_0 and the dust composition. It is therefore important to remind that *in general the size R_λ observed at a given λ does not tell us anything about the actual extend R_{out} of the torus dust mass but is a consequence of the given (radial) dust distribution.* That means that when observing the torus at a given λ , there can be a lot of “dark mass” which does not radiate at this λ , but only at longer wavelengths. The best sign for a “real” outer limit of the torus is a turnover in the observed torus SED at mid- to far-IR wavelengths. This turnover would indicate that either there is no more dust at distances which are larger than the wavelength-corresponding distance (e.g. estimated from thermal equilibrium) or the AGN radiation at the corresponding distance

Table 3. Approximate minimum outer torus radius R_λ (in units of r_{sub}) that needs to be used in models to avoid significant cut-off effects, depending on a and λ .

λ	$a = -0.5$	$a = -1.0$	$a = -1.5$	$a = -2.0$
$8 \mu\text{m}$	30	20	10	5
$13 \mu\text{m}$	50	35	20	8
$20 \mu\text{m}$	80	50	25	10
$30 \mu\text{m}$	100	80	30	15

is completely blocked so that it does not heat the dust any further, and one may define the outward extent of the torus accordingly.

A direct consequence for modeling is that R_{out} has to be properly selected rather than left as a free parameter. If, for a given dust distribution, R_{out} is too small, the brightness distribution will be cut-off at some radius and the SED breaks at some wavelength. Unless one has reasons to introduce such an artificial cut-off, it should be taken care that R_{out} is chosen in a way that it does not cut-off the brightness distribution and SED for the wavelengths of interest. An estimate for

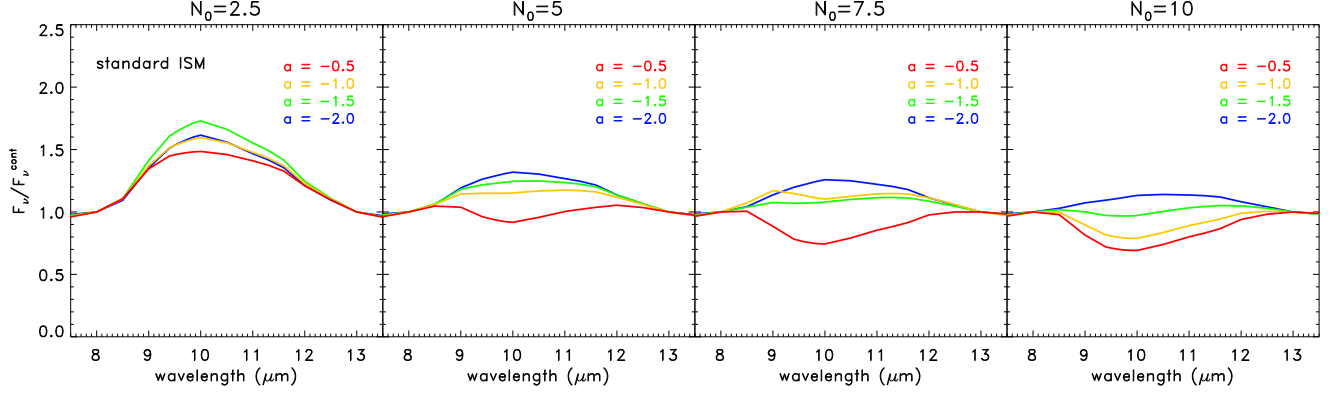


Fig. 10. Continuum-normalized $10\ \mu\text{m}$ model silicate features in type-2 AGN (inclination angle $i = 90^\circ$) for different mean number of clouds in equatorial line-of-sight N_0 and radial power-law indices a , using the ISM standard dust composition. From left to right, the panels show an increasing mean number of clouds in the equatorial line-of-sight, $N_0 = 2.5, 5, 7.5,$ and 10 , respectively. In each panel, we plot SEDs of a representative random cloud distribution for radial power law indices $a = -0.5$ (red), -1.0 (yellow), -1.5 (green), and -2.0 (blue).

this minimum size R_λ can be obtained from a simplified view of type-1 tori. Similar to the description in Sect. 2.5, we can characterize the emission of the torus with infinite extension as $L_\nu^\infty = 2\pi N_0 h \int_{r_{\text{sub}}}^\infty S_\nu(r) \eta_r r dr \propto \int_{r_{\text{sub}}}^\infty S_\nu(r) r^{a+1} dr$, where $S_\nu(r)$ is the distance- and temperature-dependent source function of a dust cloud. In a similar way, the emission $L_\nu^{R_{\text{out}}}$ with a torus size $R_{\text{out}} < \infty$ can be defined. Ideally, one would simulate cloud source functions up to infinity distance from the AGN so that no cut-off occurs. However, since computation time is limited, we propose to set R_{out} in a way that at least 95% of the infinity intensity is present in the model, i.e. $L_\nu^{R_{\text{out}}}/L_\nu^\infty \geq 0.95$. In this framework R_{out} depends on the wavelength-range that has to be modeled. In Table 3, we list minimum outer radii R_λ depending on the wavelength λ and the radial power-law index a . As expected, from $a = -0.5$ to $a = -2.0$ the emission becomes more compact and, consequently, at a given wavelength the emission region size and required R_{out} becomes smaller.

If the model is used to constrain the radial dust distribution around an AGN, e.g. by modeling its near- to mid-IR SED, the appropriate R_{out} for the longest wavelength sets the *lower limit* of the radial extend of the dust torus, if no torus cut-off is present in the object. Thus, we would suggest to characterize a torus or torus model as “compact” or “extended” rather by its radial dust distribution power-law index a than by the apparent size at a given wavelength (see also Sect. 3.5.2). While the above discussion was focused on type 1 tori, we note that in type 2 AGN, any effects on the apparent size of an object become much more pronounced since obscuration effects influence the SED and brightness distribution. Thus, it may be worthwhile setting the model R_{out} slightly larger than for type 1 AGN.

3.4. The radial dust distribution and its influence on type 2 AGN data

In type-2 AGN, the torus is seen more or less edge-on. The classification of an AGN as “type 2” is usually based on the absence of broad lines to optical hydrogen emission lines. Presumably, this absence is caused by torus dust obscuration of the BLR, and commonly goes in line with high Hydrogen column densities, N_{H} , in the X-rays. However, we would like to point out that the line-of-view to the BLR or X-ray emission region is differ-

ent from the line-of-view to the IR emitting dust clouds in the clumpy torus. Thus, despite the general trend of stronger silicate emission features with increasing N_{H} , no tight correlation can be expected.

In Fig. 9, we show model SEDs for a type 2 orientation with inclination $i = 90^\circ$. As in Fig. 6, the columns show increasing $N_0 = 2.5, 5, 7.5,$ and 10 from left to right. The rows represent results for the standard ISM, ISM large grains, and Gr-dominated dust, from top to bottom. The different colored lines are SED for $a = -0.5, -1.0, -1.5,$ and -2.0 . Compared to the low inclinations, the type-2-SEDs are redder and show less emission in the near-IR region, due to obscuration of the inner hot emission region. Some interesting result is that, despite the edge-on view of the torus, many model SEDs show silicate *emission* features. This is highlighted in more detail in Fig. 10. Here, the silicate features for ISM standard dust at torus inclination $i = 90^\circ$ have been isolated in the same way as described for the type 1 orientations. Actually, only models with flat dust distributions $a = -0.5 \dots -1.0$ and/or $N_0 \geq 5$ show the silicate feature in absorption. If the radial dust distribution is steep, most of the emission is still coming from inner hotter regions which are producing a silicate emission feature, since the emission strength depends on the temperature. It is also evident in Fig. 9 that the ISM large grain composition does not show any silicate absorption feature because of efficient obscuration due to the high optical depth in the IR. For the Gr-dominated dust, only the flattest distributions with high N_0 show weak absorption features.

Since type 2 orientations are dominated by obscuration, the properties of individual clouds – mainly τ_ν – play a role in the radiative transfer in addition to the torus parameters at-large. For the presented clouds at $\tau_\nu = 50$ but with different dust compositions, we already noted that the optical depths τ_{Si} within the silicate feature are quite different, ranging from optically thin to optically thick (see Sect. 2.4). Thus, by comparing the modeled torus silicate features for the different clouds, we can also analyze the effect of different cloud optical depths τ_{Si} on the torus SED. As shown in Fig. 9, ISM large grain dust shows only silicate emission features for $i = 90^\circ$. Since, however, silicate features *are* seen in absorption in type 2 AGN, this tells us that τ_{Si} (and maybe also τ_ν) of the clouds possibly cover only a spe-

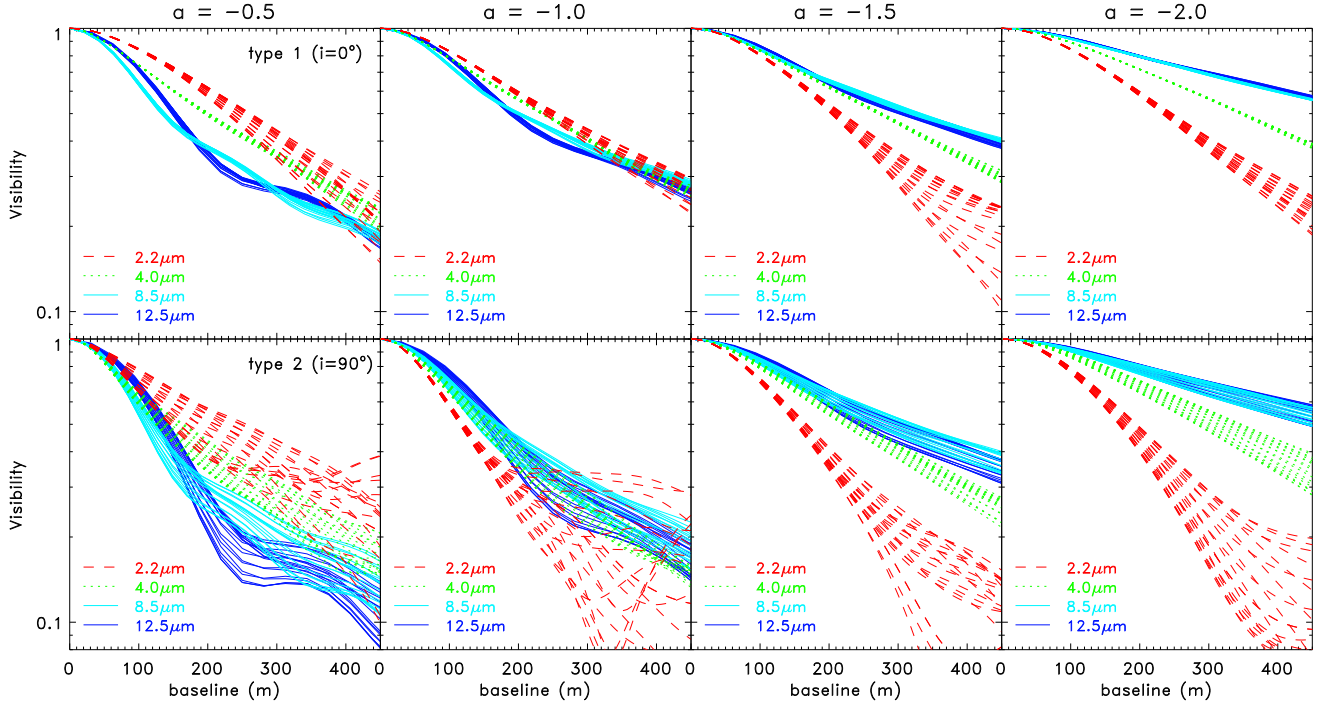


Fig. 11. Dependence of the model visibility on the baseline for an AGN at 15 Mpc distance and a sublimation radius (= near-IR reverberation radius) of 0.025 pc. Each column represents simulation results for a different radial power law index $a = -0.5, -1.0, -1.5,$ and -2.0 , respectively, (top: type 1 AGN at $i = 0^\circ$; bottom: type 2 AGN at $i = 90^\circ$) with constant $N_0 = 5$ and $R_{\text{out}} = 50$ (see Table 3). In each panel, we show visibility curves at 2.2 (red-dashed lines), 4.0 (green-dotted lines), 8.5 (light-blue solid lines), and 13.5 μm (dark-blue solid lines). The different lines per wavelength reflect the position-angle dependence of the visibility and can also be taken as a proxy for the variance that can be expected for different random arrangements of clouds (see text for details).

cific range as realized in the standard ISM and Gr-dominated dust configurations.

In conclusion, the clouds with ISM standard dust and $\tau_V = 50$ are apparently showing the overall expected torus SED properties for type 1 and type 2 AGN. Thus, these clouds can be used as a starting point for modeling actual data, and we will use them as reference in the rest of the paper.

3.5. Interpreting IR interferometry of AGN

Due to the mas-spatial scales involved in torus observations, it is difficult to spatially resolve the torus. The most promising tool for this task is IR interferometry, which was already successfully used for a number of nearby objects (e.g. Wittkowski et al. 2004; Weigelt et al. 2004; Jaffe et al. 2004; Tristram et al. 2007; Beckert et al. 2008; Tristram et al. 2009). However, except for reconstructed images of NGC 1068 obtained from Speckle interferometry (Weigelt et al. 2004), long-baseline interferometry usually provides spatial information coded as Fourier space observables, i.e. phase and visibility information for a given (projected) baseline and position angle. While the object’s phase is important for image reconstruction, the visibility contains the fundamental spatial information about the object (size, elongation). This information can be used as complementary to total flux SEDs, in particular if for a given wavelength both total and correlated fluxes are available.

The figures in the following subsections are simulated for an AGN at 15 Mpc distance with an inner radius $r_{\text{sub}} = 0.025$ pc.

They can be used as predictions for any AGN by re-scaling the x -axis baseline scale according to

$$BL_{\text{AGN}} = BL_{\text{model}} \cdot \left(\frac{D_{A;15}}{r_{0.025}} \right) \quad (9)$$

where $D_{A;15}$ is the AGN’s angular-diameter distance in units of 15 Mpc and $r_{0.025}$ is the reverberation/sublimation radius in units of 0.025 pc.

3.5.1. The baseline-dependence of the visibility

As shown in literature, adding interferometric information is very constraining for modeling the dust distribution of the torus. In particular, small-scale position-angle-dependent variations of the visibility for a given baseline and wavelength seem to be clear evidence for the clumpy structure of the torus (Hönig et al. 2006; Schartmann et al. 2008). However, interferometry constrains quite direct information about the radial intensity distribution of the torus emission: When observing almost face-on-projected type 1 AGN, no significant position-angle change of the visibility is expected. Thus, if data for different baseline lengths (corresponding to different resolution scales) is available, we have a direct and model-independent access to the surface brightness distribution I_s of the torus (see also Kishimoto et al. 2009). As shown in previous sections, $I_s \propto \xi_v \sigma_s$ primarily depends on a and to some degree on N_0 . By modeling the baseline- and wavelength-dependence of the visibility, we will be able to tightly constrain the radial dust distribution, mostly independent of SED and silicate feature modeling.

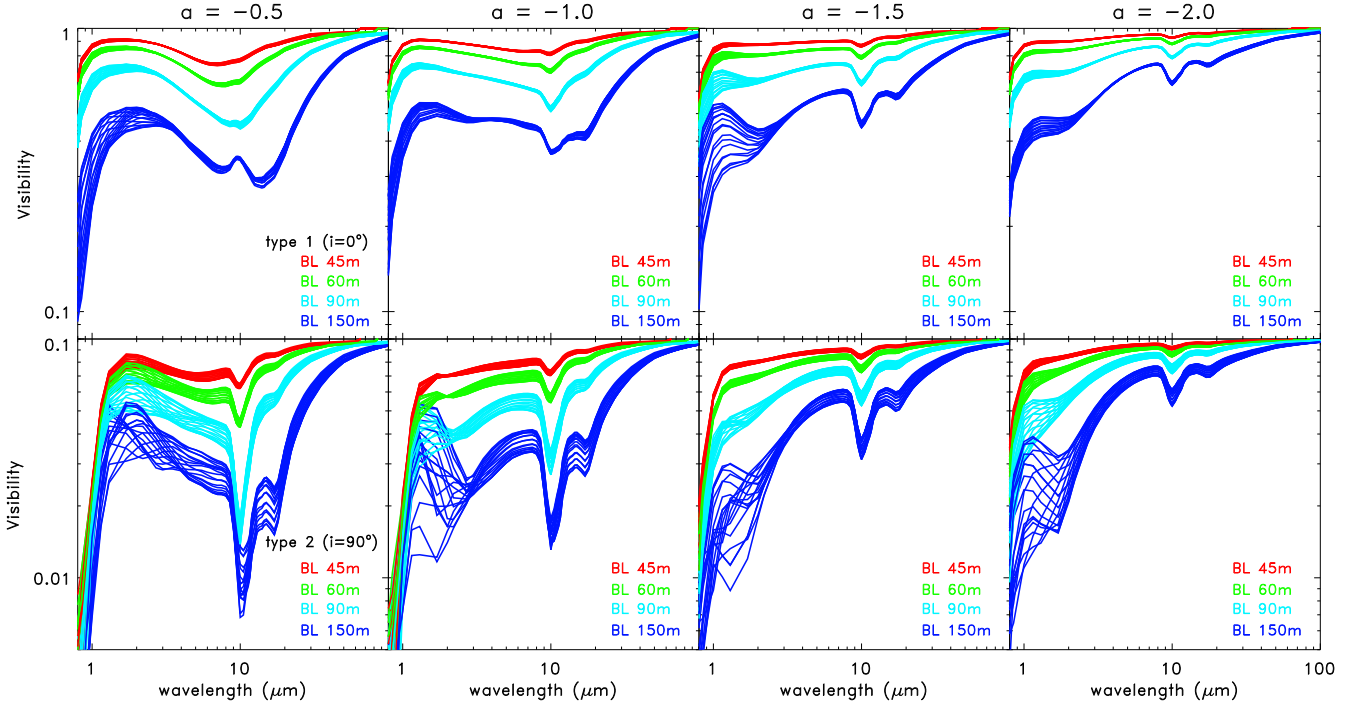


Fig. 12. Wavelength-dependence of the model visibilities for different baselines for an AGN at 15 Mpc distance and a sublimation radius (= near-IR reverberation radius) of 0.025 pc. Each row represents simulation results for different radial power law index a (top: type 1 AGN at $i = 0^\circ$; bottom: type 2 AGN at $i = 90^\circ$) with constant $N_0 = 5$ and $R_{\text{out}} = 50$ (see Table 3). In each panel, we show visibility curves for baseline lengths 45 m (red lines), 60 m (green lines), 90 m (light-blue lines) and 150 m (dark-blue lines). The different lines per wavelength reflect the position-angle dependence of the visibility and can also be taken as a proxy for the variance that can be expected for different random arrangements of clouds (see text for details).

In Fig. 11, we show the baseline-dependence of the visibility for four different wavelengths. The wavelengths have been selected to be in line with current and future interferometric instruments at the VLT and the Keck interferometers: the K -band at $2.2\mu\text{m}$ (e.g. VLTI/AMBER), $4.0\mu\text{m}$ in the L/M -band region (e.g. KI or future VLTI/MATISSE), and 8.5 and $12.5\mu\text{m}$ in the N -band (e.g. VLTI/MIDI). For the simulations, we use $N_0 = 5$ and $R_{\text{out}} = 50$ and present results for different radial power law indices $a = -0.5, -1.0, -1.5,$ and -2.0 . The top and bottom rows in Fig. 11 show $i = 0^\circ$ and $i = 90^\circ$, respectively. For all wavelengths the variation with position angle due to clumpiness is shown (in steps of 10°). This can also be used as a proxy of what kind of variations can be expected between different random arrangements of clouds, as discussed in Hönig et al. (2006).

We will first concentrate on the type 1 case where the observed visibilities can be directly used to constrain the dust distribution. For the shown baseline lengths from 0–450 m, the K -band visibilities have an overall similar shape. For instance, the K -band visibility at 200 m is ~ 0.6 , independent of the power law index a . At 400 m, the visibilities have dropped to around 0.2 in all cases. The actual difference between different a values, as well as the position-angle variance, are mostly caused by the random arrangement of the clouds and only to a minor degree by a change of the parameter a (or N_0). This can be understood since most the K -band emission is originating only from the hot dust which is located in the innermost region of the torus, regardless of the actual torus-internal obscuration or dust distribution. However, since individual dust clouds are optically thick in the K -band (see Sect. 2.4), variations of the vis-

ibilities depend on the actual clouds’ placements, for different position angles or the general arrangement of the clouds in the torus. For the other wavelengths shown in Fig. 11, the individual clouds are optically thin and the variations with position angle – and, thus, also the expected variations between random cloud arrangements – is much smaller. The variations still seen are coming from a combination of “clumping of clumps” in the torus, resulting in both stronger local emission and absorption, or from “holes” in the distribution, mostly if N_0 is very small. From this analysis, we can draw an interesting first conclusion: The strength of the position-angle dependence of the visibility is related to properties of the clouds. This concerns, in particular, the optical depth of the clouds which is related to the cloud dust mass or geometrical properties and the dust composition. We note, however, that the characteristics of position-angle/cloud-arrangement variations are highly degenerate with typical cloud size, cloud optical depth, and the dust composition, so that it is difficult to constrain any of these parameters from observations individually.

Since we already noted that the K -band visibility curve is more or less the same for different a , it can be used as a reference for the other wavelengths. As can be seen in Fig. 11, the baseline-dependence of the visibility changes with a for the presented wavelengths other than $2.2\mu\text{m}$: the $4\mu\text{m}$ visibility curve is slightly below the K -band line for $a = -0.5$ and -1.0 and slightly above for $a = -1.5$ and -2.0 , with a total increase from $V_{4\mu\text{m}} = 0.5$ to 0.75 at 200 m. On the other hand, the N -band visibilities change much stronger, increasing from $V_{12.5\mu\text{m}} = 0.35$ to 0.8 at 200 m. The basis of these behaviour is the spatial regions

and temperatures involved in emitting light at the given wavelengths. At short wavelengths, only hot dust contributes to the emission and no light will be emitted from cool dust. This makes the emission region small, no matter how the dust is distributed. In a simplified picture of a type 1 AGN, we expect that only a very small ring is seen, approximately with the size corresponding to the equilibrium temperature peaking at this wavelengths. At longer wavelengths both hot and cooler cloud contribute to the flux. Thus, the emission region becomes more extended. The actual extension, however, depends on how the dust is radially distributed. If the density is steeply decreasing outwards, the size is still small and comparable to only hot emission. If the density distribution is flat, larger distances contribute significantly and the size is much more extended than for hot emission.

The described principles are also valid for type 2 objects. However, in type 2 AGN obscuration within the torus becomes more important. In the bottom row of Fig. 11, we show the baseline-dependence of the visibility for an inclination angle $i = 90^\circ$, i.e. edge-on as in type 2 AGN. Since clouds at larger radii along our line-of-sight obscure clouds at smaller radii where most of the hot emission is originating, the tori look more extended. Thus, the visibilities for a given baseline and wavelengths are generally smaller than in the type 1 case. Since obscuration plays an important role, the small-scale variations of the visibility are stronger. In addition and as expected, the tori show elongation along the mid-plane (see also Fig. 5) which is responsible for a large fraction of the position-angle dependence of the visibility shown in Fig. 11 (bottom). Similar to the type-1 case, the K -band visibility shows the strongest small-scale visibility variation because the clouds are optically thick. Again, we note that the position-angle dependence in Fig. 11 (bottom) can be used as a proxy for the expected variations when using a different random arrangement of clouds. The essential dependence of the visibility curves on wavelength are also comparable to the type 1 case: Longer wavelengths show a stronger change from steep to flat for a changing from -0.5 to -2.0 . It is interesting to note that from $a = -0.5$ to -2.0 , the type 2 AGN visibilities become very similar to type 1 AGN. This goes in line with the a -dependence of the total SEDs as shown previously. As previously noted, this can be understood when considering that in the steep cases, most of the dust is located within few sublimation radii (see also Table 3). Thus, the overall emission is dominated by hot clouds without obscuration from larger scales. We note that when N_0 increases, the difference in visibility curves for a given wavelength between type 1 and type 2 AGN slightly increases, but mainly for $a = -0.5$ and $= 1.0$ where obscuration effects are more important.

In summary, as illustrated in Fig. 11, the baseline-dependence of the visibility in type 1 AGN directly traces the radial dust distribution in the torus: If the dust distribution is steep ($a = -1.5$ or -2.0), the baseline-dependence of the visibility is comparably flat, and vice versa, and the effect becomes stronger for longer wavelengths. In principle, this also accounts to type 2 AGN, but obscuration effects and small-scale visibility variations make the a -dependence of the visibility less obvious. Although we only show results for $N_0 = 5$, we note that these conclusions are mostly independent of N_0 for the range of $N_0 = 2.5$ to 10 that we investigate in this paper.

3.5.2. The wavelength-dependence of the visibility

In Fig. 11, we can see that for the “extended” tori with $a = -0.5$ and -1.0 , the visibilities curves at wavelengths longer than $2.2\mu\text{m}$ are below the K -band visibility curve. In other words,

the wavelength-dependent size of the torus grows faster than the wavelength-dependent resolution decreases for a given baseline. On the other hand, the “compact” tori with $a = -1.5$ and -2.0 show the opposite behavior, i.e. the long wavelength visibility curves are above the K -band curve. Of course, this reflects the fact that most of the dust is confined to the inner torus region, making the apparent size small at all wavelengths. While this finding is true for both type 1 and type 2 orientations, it is much more obvious in rather face-on geometries where obscuration effects do not play a significant role.

Instead of looking at the baseline-dependent visibility at different wavelengths, we can also compare the wavelength-dependence of the visibility for given baselines. In Fig. 12 we show visibilities in the 1 to $100\mu\text{m}$ range for both type 1 (top row) and type 2 (bottom row) orientations of the torus. As in the previous figure, we plot curves for $a = -0.5, -1.0, -1.5,$ and -2.0 (from left to right row), $N_0 = 5$ and $R_{\text{out}} = 50$. Each panel contains simulations for baseline lengths of 45 m (red), 60 m (green), 90 m (light blue), and 150 m (dark blue). For each configuration, various lines illustrate the position-angle dependence. As already noted for Fig. 11, for a given baseline length the compact tori have decreasing visibility with wavelength from the near-IR to about $20\mu\text{m}$. At longer wavelengths, the visibility increases again. The increase for long baselines is caused, to a minor extent, by the limited $R_{\text{out}} = 50$ which might result in a slight cut-off (see Sect. 3.3 and Table 3), but to greater extent is the result of torus internal obscuration which shields clouds at larger radii from AGN light or short-wavelength dust re-emission. Thus, clouds at these distances do not contribute anymore to the IR torus emission. This goes in line with a turnover in SED at the same wavelengths as discussed in previous sections. For compact tori, the visibilities keep increasing from the near-IR to the mid-IR and up to $100\mu\text{m}$. For type 1 orientations, the transition between decreasing and increasing visibility is occurring somewhere between $a = -1.0$ and -1.5 , and we note that it is more or less independent of N_0 within the studied range. For type 2 AGN, the change occurs just around $a = -1.0$. However, obscuration effects (and the choice of N_0) have a stronger influence as illustrated by the visibility variations for different position-angles in the optically thick regions in the near-IR and at short wavelengths. Nevertheless, the change of the wavelength-dependent visibility slope with a opens an interesting possibility to narrowly constrain the radial distribution of the dust, at least in type 1 AGN: By obtaining interferometric visibilities for an AGN at 2 different wavelengths for the same baseline length – preferably one visibility point in the near-IR, one in the mid-IR – it is possible to constrain the radial dust distribution index a or, at least, characterize the radial dust distribution as “extended” ($a \geq -1.0$) or “compact” ($a \leq -1.5$). Such experiments can, for example, be done using the UT telescope baseline configurations at the VLTI in combination with the AMBER and the MIDI instruments. While type 1 AGN observations are much more revealing, looser constraints on the dust distribution can be imposed on individual type 2 AGN. On the other hand, since the number of interferometrically-observable type 2 AGN is probably larger, studies of several obscured AGN will be quite revealing as well. In addition, if constraints on the dust distribution from type 1 AGN are used for modeling of type 2s, it will be possible to constrain N_0 and maybe the vertical dust distribution.

At around $10\mu\text{m}$ in the visibility curves of Fig. 12, a change of the visibility within the silicate feature of face-on and edge-on orientations can be seen. This imprint of the silicate feature on the visibilities is commonly interpreted as a clear signpost

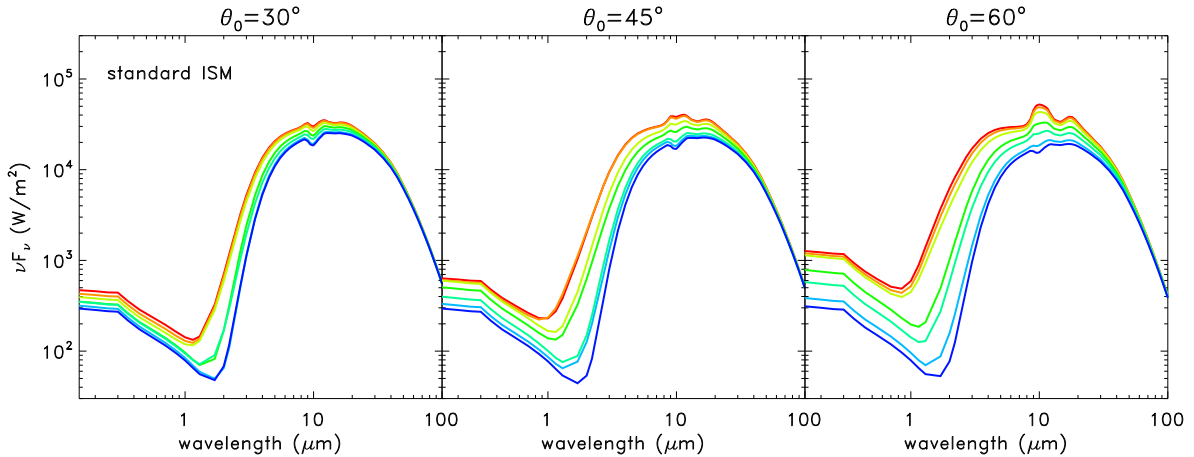


Fig. 13. Model SEDs of AGN tori for different half opening angles θ_0 . From the left to the right panel we present $\theta_0 = 30^\circ$, 45° and 60° . Each panel shows inclination angles from $i = 0^\circ$ (type 1; red) to 90° (type 2; blue) in steps of 15° . For the simulations, we fixed $a = -1.0$, $N_0 = 7.5$, and $R_{\text{out}} = 50$, and used the standard ISM composition.

of clumpiness in the torus, since smooth dust distributions are apparently not showing this feature in the visibility spectrum (Jaffe et al. 2004; Schartmann et al. 2005; Hönig et al. 2006). On the other hand, a silicate absorption feature is prominently displayed in interferometric data of NGC 1068 (Jaffe et al. 2004; Poncelet et al. 2006; Raban et al. 2009). As seen in Figs. 6, 7, 9, & 10, and discussed in Sects. 3.2 & 3.4, the actual strength of the feature and whether it is seen in emission or absorption in the SED is depending on a combination of parameters a and N_0 , and the dust composition. The situation for the silicate feature in the interferometric data is even more complex since the feature contains not only flux variations with respect to the continuum but also *variations in the emission region*. Thus, a silicate feature in the visibilities or correlated fluxes cannot be directly associated with obscuration or the source function at/within a certain region but involves different spatial scales. As a result, physical properties of the torus are highly decoded in the interferometric silicate features. Another problem is that the interferometric silicate absorption and emission feature as shown in Fig. 12 are not very strong: In type 1 AGN, the visibility change from continuum to feature center is generally of the order of 0.1-0.15, and in type 2 AGN in might be up to 0.2-0.25 at maximum. Thus, visibility or correlated flux accuracies down to these levels are required to detect the features.

3.6. The opening angle of the torus

In all previous simulations of Sect. 3, we assumed that the half-opening angle θ_0 of the torus is 45° . This assumption is based on type-1/type-2 number counts (e.g. Maiolino & Rieke 1995; Lacy et al. 2004; Martínez-Sansigre et al. 2006) and direct observations of extended gas emission in nearby AGN (e.g. Hicks et al. 2009). As such, $\theta_0 = 45^\circ$ should capture the average property of the dust torus. However, supporting the torus scale height $h \sim 1$ poses some difficulty on theoretical models of dust tori, and additional energy input from accretion, supernovae, winds, or radiation pressure is assumed (e.g. Beckert & Duschl 2004; Elitzur & Shlosman 2006; Krolik 2007; Schartmann et al. 2009). It has been proposed that in some objects the dust tori are significantly flatter (e.g. Mason et al. 2009) or thicker (e.g. Levenson et al. 2007) than average, which may be connected to

different kinds of accretion support, starbursts, and/or associated AGN luminosities and Eddington ratios (Vollmer et al. 2004; Beckert & Duschl 2004; Hönig & Beckert 2007; Vollmer et al. 2008).

We analyzed the impact of a larger and smaller half-opening angle on the SED and visibilities of type 1 and type 2 torus models. In Fig. 13 we compare model SEDs with ISM standard dust for $\theta_0 = 30^\circ$, 45° , and 60° (from left to right). In each panel, we show torus inclinations from $i = 0^\circ$ (face-on; red) to 90° (edge-on; blue), in steps of 15° . Compact tori with $a = -1.5$ and -2.0 are not showing too much dependence on the θ_0 since most of the clouds are residing in the innermost torus region. Thus, we used $a = -1.0$ for the simulations to better illustrate effects of varying θ_0 . In addition, $N_0 = 7.5$, and $R_{\text{out}} = 50$ have been fixed.

A first interesting result is that the selection of θ_0 seems to have very little effect on type 2 SEDs. For the θ_0 values from 30° to 60° shown in Fig. 13, the edge-on SEDs are literally the same in terms of near-IR color and silicate feature depth. The only difference between the $i = 90^\circ$ SEDs are the absolute flux levels which are higher in the thicker torus ($\theta_0 = 30^\circ$). This has to do with the way the torus emission is re-distributed: In a flat torus, radiation which is emitted in the torus mid-plane into the pole-on direction escapes almost undisturbed. Thus, the low- i SEDs for $\theta_0 = 60^\circ$ show hotter emission (see near-IR slope and silicate emission feature) and there is a large flux difference between face-on and edge-on SEDs. In the thick torus, obscuration effects are also significant in more or less pole-on directions, so that the re-radiation in general does not directly escape but is again absorbed and re-emitted into all directions. This reduces the emission in face-on SEDs for $\theta_0 = 45$ and 30° and makes the over-all torus emission more isotropic. Consequently, the silicate emission feature in type-1 orientations becomes weaker for decreasing θ_0 and may even turn into absorption.

The side effect of this θ_0 -dependence in face-on viewing angles is that constraining a only from the SED of a type 1 AGN becomes ambiguous: Similar SEDs can be reproduced for flat a and large θ_0 as well as for a steep a and small θ_0 . However, in most nearby AGN we have constraints on the half-opening angles from observations of the narrow-line regions, e.g. the ionization cones in $[\text{O III}]$ or $\text{H}\alpha$. Moreover, as mentioned previously, statistical considerations imply that θ_0 of the typical AGN

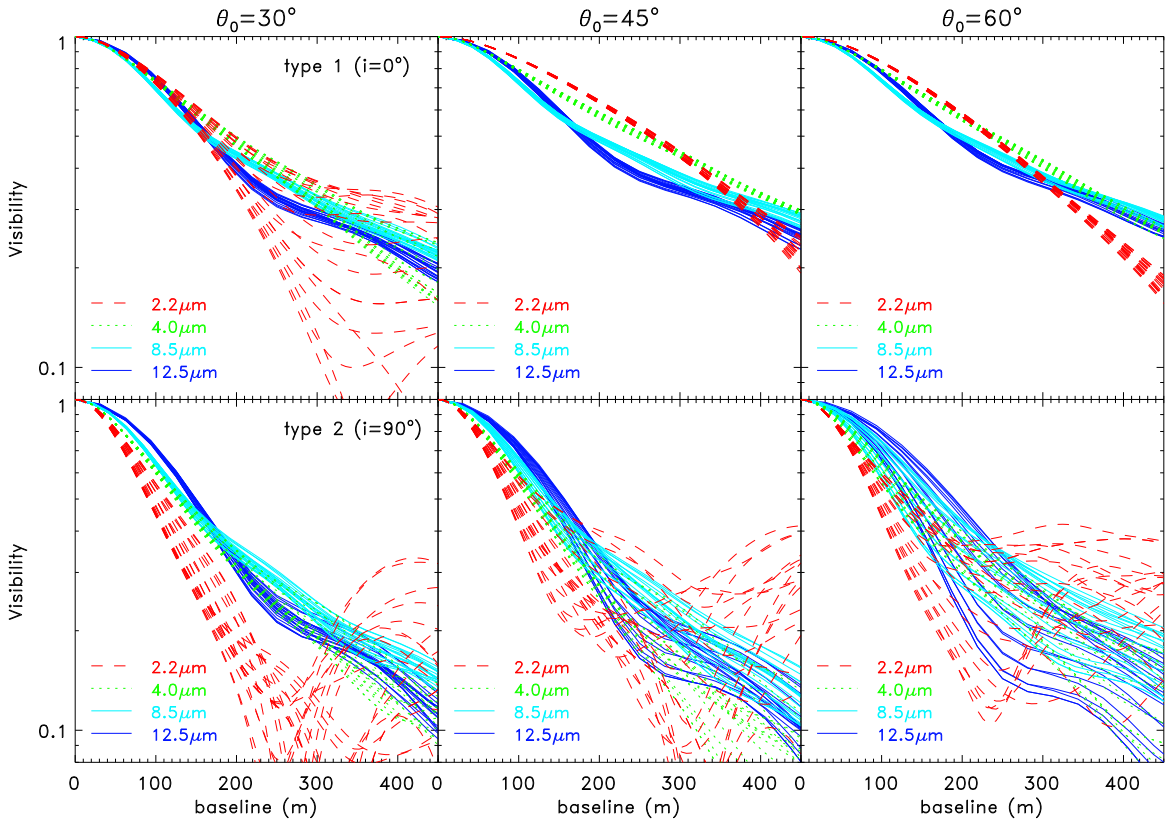


Fig. 14. Dependence of the model visibility on the baseline for an AGN at 15 Mpc distance and a sublimation radius (= near-IR reverberation radius) of 0.025 pc. From left to right, each column represents simulation results for a different half opening angle $\theta_0 = 30^\circ$, 45° , and 60° (top: type 1 AGN at $i = 0^\circ$; bottom: type 2 AGN at $i = 90^\circ$) with fixed $a = -1.0$, $N_0 = 7.5$ and $R_{\text{out}} = 50$. In each panel, we show visibility curves at 2.2 (red-dashed lines), 4.0 (green-dotted lines), 8.5 (light-blue solid lines), and 13.5 μm (dark-blue solid lines). The different lines per wavelength reflect the position-angle dependence of the visibility and can also be taken as a proxy for the variance that can be expected for different random arrangements of clouds.

is near 45° , so that, on average, fixing $\theta_0 = 45^\circ$ should result in a meaningful constraint for a .

Another way around the parameter degeneracy is using interferometric data. In Fig. 14, we show the baseline-dependent visibility for type-1 and type-2 viewing angles for different wavelengths. From left to right, model visibilities are presented for $\theta_0 = 30^\circ$, 45° , and 60° (top: $i = 0^\circ$; bottom: $i = 90^\circ$). As in Fig. 13 we used $a = -1.0$, $N_0 = 7.5$, and $R_{\text{out}} = 50$. For the type 1 SEDs, the baseline-dependence of the visibilities is more or less independent of the selection of the half-opening angle. For all 3 θ_0 -values shown, the visibilities up to 450 m are the same within 0.05 for $\lambda \geq 4 \mu\text{m}$. Thus, visibilities seem to be a good tool to break the parameter degeneracy in SED models. For 2.2 μm , the $\theta = 30^\circ$ model visibilities are steeper than for $\theta_0 = 30^\circ$ and 45° , and show strong variations with position angles. The reason is the much stronger torus-internal obscuration and the fact that the dust clouds are optically thick at 2.2 μm . As such the torus starts to resemble type 2 characteristics (see Sec. 3.5.1).

In the edge-on view on the torus, the average baseline-dependent visibility for each wavelength is also roughly independent of the selection of θ_0 . However, the position-angle dependence changes a lot. While the visibilities show more or less the same characteristics for $\theta_0 = 30^\circ$ and 45° , the visibilities change a lot for $\theta_0 = 60^\circ$ when varying the position angle from the direction parallel to the torus mid-plane (lowest visibility

curves for each wavelength) to perpendicular to the mid-plane (highest visibility curves). This is quite understandable since for large opening angles, the torus becomes very flat. Thus, the emission region size is more extended along the mid-plane than perpendicular to it.

In summary, the half-opening angle θ_0 of the torus has some influence on the model SEDs – mostly on type 1 viewing-angles – and results in some parameter degeneracy with a when modeling data. On the other hand, this degeneracy can be overcome when using interferometric visibilities which are, in the type 1 cases, mostly independent on θ_0 . In addition, large half-opening angle tori have a stronger position-angle dependence of the visibilities. We conclude, however, that fixing $\theta_0 = 45^\circ$ when modeling real data should provide a meaningful constraint on a , unless no better information on θ_0 can be obtained, e.g. from ionization cone shapes.

3.7. The influence of the accretion disk

The presented torus models do not include any accretion disk contribution. For type 2 AGN, it is safe to conclude that most of the observed IR flux is coming from the dust torus since, by definition, the accretion disk has to be obscured. On the other hand, depending on wavelength, the accretion disk might contribute to the overall AGN IR flux in type 1 AGN.

Recently, we presented an analysis of the near-IR emission of nearby type 1 AGN (Kishimoto et al. 2007). We used a color-color diagram to disentangle the hot dust emission from the accretion disk power law spectrum extending from optical wavelengths into the IR. A simultaneous power-law+black-body fit suggested that the accretion disk contribution to the AGN near-IR is around 10–50% in the H -band and only 5–25% in the K -band. The decrease of accretion disk contribution with wavelength is consistent with the recent observation of the blue tail of the near-IR accretion disk emission (Kishimoto et al. 2008) which suggests that for any wavelength longer than $2\ \mu\text{m}$, the accretion disk has marginal effect on SED and interferometry. In Kishimoto et al. (2007), we also showed that a possible 20% accretion disk contribution in the K -band increases the visibilities by at worst ≤ 0.1 for the longest baseline shown in Fig 12. Since the position-angle variations in the near-IR are of the same magnitude, any accretion disk contribution will be hidden under these variations. Thus, we refrained from adding the accretion disk contribution to the presented figures and note that for interpretation of near-IR interferometry, a case-to-case analysis based on the color-color diagram should constrain to what degree the accretion disk has to be taken into account.

4. Summary and conclusion

We presented modeling results from our upgraded 3D radiative transfer model of clumpy tori and described how observations can constrain parameters of this model. First, we outlined our modeling strategy and presented results of Monte Carlo simulations of dust clouds, which are externally heated, using different dust compositions. We used standard ISM compositions with Draine&Lee and Ossenkopf silicates, respectively, and compared the cloud SEDs to simulations with a large grain composition and Graphite-dominated dust. The differences between the cloud SEDs from different dust compositions are an effect of the optical depth in the infrared and the different (Planck mean) opacities of each dust distribution which result in a slightly different temperature gradient with distance from the AGN.

In the next step, we introduced the parameters of our models and how they connect to properties of the torus, such as the volume filling factor or the cloud number density. By outlining a simplified type 1 torus model, we showed that the main parameters that have an influence on the torus SED and images are the radial dust cloud distribution power-law index a , the mean number of clouds along an equatorial line-of-sight N_0 , and the torus height described either as the scale height h or the half-opening angle θ_0 . We also noted that the cloud radii R_{cl} do not have a significant impact on the torus simulation results, while the cloud dust properties (τ_V and dust composition) will be important.

By using the pre-calculated cloud SEDs and images, we simulated torus SEDs and studied how different parameters affect the model SEDs. The SEDs are presented in a suitable way to be scaled to observations. Our main conclusions are:

- The dust clouds with standard ISM dust and Ossenkopf silicates seem to provide reasonable torus SEDs which seemingly capture the essence of recently observed IR characteristics of AGN (e.g. moderate $10\ \mu\text{m}$ silicate emission and absorption features). Moreover, we conclude that the optical depth in the IR of the dust clouds should be of the order of unity or smaller. Otherwise, the model SEDs become extremely red and the silicate emission feature is too strong.
- We note that the sublimation radius for the clouds with the ISM standard dust composition is $r_{\text{sub}} = 1.1\ \text{pc} \times$

$(L/10^{46}\ \text{erg/s})^{1/2}$. This is still ~ 2.9 times larger than what has been inferred from reverberation mapping (see Table 1). A slight modification of the presented models, where the minimum dust grain size is larger for small AGN distances, should provide better consistency between r_{τ_K} and r_{sub} .

- AGN torus models, in particular in type 1 cases, are quite sensitive to the selection of a and N_0 , and there exists some degeneracy between a and N_0 . Increasing N_0 increases the torus-internal obscuration in both radial and vertical directions. As a result, shorter wavelengths are more strongly absorbed internally, and the overall SED becomes redder. On the other hand, redder SEDs can also be obtained when distributing more dust clouds at larger distances (e.g. $a = -0.5$ or -1.0) since the dust in the torus is cooler on average. However, modeling simultaneously the $10\ \mu\text{m}$ silicate feature (more sensitive to N_0) and the continuum IR SED (more sensitive to a) allows us to constrain both parameters individually, breaking most of the degeneracy.
- Due to obscuration effect, SEDs of edge-on orientations of the torus as in type 2 AGN are less constraining for the radial dust distribution. Still, depending on the appearance of the silicate feature, they can be used to roughly characterize N_0 and provide some constraints on the characteristics of the dust clouds. Here, modeling the silicate feature in detail provides most information.
- The appearance of the silicate feature – either in absorption or emission – is not only viewing-angle dependent, but strongly influenced by a , N_0 and possibly τ_V of the cloud and the dust composition. We showed that for $\tau_V = 50$, compact dust distributions ($a = -1.5$ and -2.0) are not producing silicate absorption features for $N_0 \leq 10$. Moreover, the silicate emission features in type 1 AGN become more pronounced with decreasing N_0 and/or more compact a . From the commonly seen weak silicate emission features in type 1 AGN and silicate absorption features in type 2 AGN, we would expect that, in general, AGN dust tori should have rather extended dust distributions with $N_0 \gtrsim 5$. This claim can be tested by detailed modeling of IR observational data.
- The outer radius of the torus R_{out} cannot be constrained by IR SED modeling and better not be used as a free model parameter. In contrast, to avoid brightness distribution cut-offs, it has to be properly selected in the models. We provide a table which can be used to give lower limits on R_{out} depending on a and the observed wavelength λ .
- Varying the half-opening angle θ_0 results in some parameter degeneracy with a when modeling type 1 AGN data, while in more inclined cases θ_0 has minor influence. We suggest that using $\theta_0 = 45^\circ$ should provide a meaningful constraint on a , at least when using object samples. For individual objects, the opening angle of the NLR/ionization cone is useful to estimate θ_0 prior to SED modeling. Alternatively, interferometric information will better constrain a without too much dependence on θ_0 (see below).

From torus model images, we calculated visibilities to simulate observations with interferometers. In addition to the SEDs, these data provide spatial information at different wavelengths and at different scales depending on the baseline length. We conclude:

- In type 1 AGN, the baseline-dependence of the visibility directly traces the radial power law index a without significant influence from other parameters. The general principle is also valid for type 2 AGN, but obscuration and geometric

effects result in significant dependence of the visibility on position angle.

- By comparing visibilities at two different wavelengths (preferably one in the near-IR, one in the mid-IR) for a given baseline, one can directly conclude if the dust distribution is compact ($a \geq -1.5$) or extended ($a \leq -1.0$). This can be done for both type 1 and type 2 AGN, although type 2s are less constraining due to obscuration effects.
- Small-scale position-angle variations of the visibility are usually associated with clumpiness of the torus. We found out that the strength of these variations are controlled by (1) the optical depth τ of the cloud and, thus, also the dust composition (they are strongest if $\tau_{\lambda} \gg 1$ at the observed wavelength λ), (2) the cloud size R_{cl} , and (3) the obscuration in the torus, i.e. N_0 . It is quite difficult to constrain any of these parameter individually by observing the variations.
- The visibilities show silicate features in both type 1 and type 2 orientations. From continuum to peak, the visibility changes by 0.1–0.2. Since the silicate feature in the visibilities is the result of both changes of flux and emission region size, it cannot be directly associated with emission properties of or within a certain region. The actual strength of the feature is degenerate with several parameters.
- We showed that for type 1 AGN interferometry, the half-opening angle θ_0 has an influence on the baseline-dependent visibility only if it is small, i.e. the outflow funnel is narrow (here: $\theta_0 = 30^\circ$). Otherwise, a can be well constrained by interferometry. In type 2 AGN, θ_0 has some influence on the position-angle dependence of the visibility: While for flat distributions ($\theta_0 = 60^\circ$) the IR emission region of the torus is elongated along the mid-plane, it is more isotropic for smaller half-opening angles.

The presented models can be used as direct input for interpreting observational data. We are pleased to provide the model SEDs to interested colleagues on request. In the next papers of this series, we will apply our model to the Seyfert 1 and 2 sample of nearby galaxies for which we obtained high-spatial resolution mid-IR spectro-photometry and near-IR images (spatial resolution < 0.4 or $\lesssim 100$ pc). As discussed, such data will provide constraints on the radial dust distribution in the torus and obscuration properties. Application to interferometry of nearby AGN will be subject to following papers.

Acknowledgements. We thank P. Gandhi, K. Ohnaka, and R. Antonucci for fruitful discussion and helpful comments during evolution of this project.

References

- Antonucci, R. 1993, *ARA&A*, 31, 473
 Beckert, T., & Duschl, W. J. 2004, *A&A*, 426, 445
 Beckert, T. 2005, *MmSAI*, 76, 150
 Beckert, T., Driebe, T., Hönig, S. F., & Weigelt, G. 2008, *A&A*, 486, L17
 Bjorkman, J. E., & Wood, K. 2001, *ApJ*, 554, 615
 Draine, B. T., & Lee, H. M. 1984, *ApJ*, 285, 89
 Dullemond, C. P., & van Bemmell, I. M. 2005, *A&A*, 436, 47
 Efstathiou, A., & Rowan-Robinson, M. 1995, *MNRAS*, 273, 649
 Elitzur, M., & Shlosman, I. 2006, *ApJ*, 648, L101
 Granato, G. L., & Danese, L. 1994, *MNRAS*, 268, 235
 Hicks, E. K. S., Davies, R. I., Malkan, M. A., Genzel, R., Tacconi, L. J., et al. 2009, *ApJ*, 696, 448
 Hönig, S. F., Beckert, T., Ohnaka, K., & Weigelt, G. 2006, *A&A*, 452, 459
 Hönig, S. F., Beckert, T., Ohnaka, K., & Weigelt, G. 2007, *ASPC*, 373, 487
 Hönig, S. F., & Beckert, T. 2007, *MNRAS*, 380, 1172
 Hönig, S. F., Prieto, M. A., & Beckert, T. 2008, *A&A*, 485, 33
 Indebetouw, R., Whitney, B. A., Johnson, K. E., & Wood, K. 2006, *ApJ*, 636, 362
 Ivezić, Ž., Nenkova, M., & Elitzur, M. 1999, User Manual for DUSTY, Univ. of Kentucky internal report, accessible at <http://www.pa.uky.edu/~moshe/dusty/>
 Jaffe, W., Meisenheimer, K., Röttgering, H. J. A., Leinert, Ch., Richichi, A., et al. 2004, *Nature*, 429, 47
 Kishimoto, M., Hönig, S. F., Beckert, T., Weigelt, G. 2007, *A&A*, 476, 713
 Kishimoto, M., Antonucci, R., Blaes, O., Lawrence, A., Boisson, C., et al. 2008, *Nature*, 454, 492
 Kishimoto, M., Hönig, S. F., Tristram, K., Weigelt, G. 2009, *A&A*, 493, L57
 Königl, A., & Kartje, J. F. 1994, *ApJ*, 434, 446
 Krolik, J. H. & Begelman, M. C. 1988, *ApJ*, 329, 702
 Krolik, J. H. 2007, *ApJ*, 661, 52
 Krügel, E., *An introduction to the physics of interstellar dust*, Boca Raton 2008
 Lacy, M., Storrie-Lombardi, L. J., Sajina, A., Appleton, P. N., Armus, L., et al. 2004, *ApJS*, 154, 166
 Levenson, N. A., Sirocky, M. M., Hao, L., Spoon, H. W. W., Marshall, J. A., et al. 2007, *ApJ*, 654, L45
 Lucy, L. B. 1999, *A&A*, 344, 282
 Manske, V., Henning, T., & Men'shchikov, A. B., *A&A*, 331, 52
 Maiolino, R., & Rieke, G. H. 1995, *ApJ*, 454, 95
 Martínez-Sansigre, A., Rawlings, S., Lacy, M., Fadda, D., Jarvis, M. J., et al. 2006, *MNRAS*, 370, 1479
 Mason, R. E., Levenson, N. A., Shi, Y., Packham, C., Gorjian, V., et al. 2009, *ApJ*, 693, L136
 Miller, J. S. & Antonucci, R. R. J. 1983, *ApJ*, 271, L7
 Moran, C. M., Barth, A. J., Kay, L. E., & Filippenko, A. V. 2000, *ApJ*, 540, L73
 Natta, A., & Panagia, N. 1984, *ApJ*, 287, 228
 Nenkova, M., Ivezić, Ž., & Elitzur, M. 2002, *ApJ*, 570, L9
 Nenkova, M., Sirocky, M. M., Ivezić, Z., Elitzur, M. 2008, *ApJ*, 685, 147
 Nenkova, M., Sirocky, M. M., Nikutta, R., Ivezić, Z., Elitzur, M., *ApJ*, 685, 160
 Ohnaka, K., Driebe, T., Hofmann, K.-H., Leinert, C., Morel, S., et al. 2006, *A&A*, 445, 1015
 Ossenkopf, V., Henning, T., & Mathis, J. S. 1992, *A&A*, 261, 567
 Pier, E. A., & Krolik, J. H. 1993, *ApJ*, 418, 673
 Poncelet, A., Perrin, G., & Sol, H. 2006, *A&A*, 450, 483
 Raban, D., Jaffe, W., Röttgering, H., Meisenheimer, K. & Tristram, K. R. W. 2009, *MNRAS*, 394, 1325
 Risaliti, G., Elvis, M., Fabbiano, G., Baldi, A., Zezas, A., & Salvati, M. 2007, *ApJ*, 659, L111
 Schartmann, M., Meisenheimer, K., Camenzind, M., Wolf, S., & Henning, T. 2005, *A&A*, 437, 861
 Schartmann, M., Meisenheimer, K., Camenzind, M., Wolf, S., Tristram, K. R. W., & Henning, T. 2008, *A&A*, 482, 67
 Schartmann, M., Meisenheimer, K., Klahr, H., Camenzind, M., Wolf, S., & Henning, T. 2009, *MNRAS*, 393, 759
 Scott, J. E., Kriss, G. A., Brotherton, M., Green, R. F., Hutchings, J., et al. 2004, *ApJ*, 615, 135
 Shi, Y., Rieke, G. H., Hines, D. C., Gorjian, V., Werner, M. W., et al. 2006, *ApJ*, 653, 127
 Suganuma, M., Yoshii, Y., Kobayashi, Y., Minezaki, T., Enya, K. et al. 2006, *ApJ*, 639, 46
 Swain, M., Vasisht, G., Akeson, R., Monnier, J., Millan-Gabet, R., et al. 2003, *ApJ*, 596, L163
 Tacconi, L. J., Genzel, R., Blietz, M., Cameron, M., Harris, A. I., & Madden, S. 1994, *ApJ*, 426, L77
 Tristram, K. R. W., Meisenheimer, K., Jaffe, W., Schartmann, M., Rix, H.-W., et al. 2007, *A&A*, 474, 837
 Tristram, K. R. W., et al. 2009, *A&A*, submitted
 Urry, C. M., & Padovani, P. 1995, *PASP*, 107, 803
 Vanden Berk, D. E., Richards, G. T., Bauer, A., Strauss, M. A., Schneider, D. P., et al. 2001, *AJ*, 122, 549
 Vollmer, B., Beckert, T., & Duschl, W. J. 2004, *A&A*, 413, 949
 Vollmer, B., Beckert, T., & Davies, R. I. 2008, *A&A*, 491, 441
 Weigelt, G., Wittkowski, M., Balega, Y. Y., Beckert, T., Duschl, W. J., et al. 2004, *A&A*, 425, 77
 Wittkowski, M., Balega, Y., Beckert, T., Duschl, W. J., Hofmann, K.-H., & Weigelt, G. 1998, *A&A*, 329, L45
 Wittkowski, M., Kervella, P., Arsenault, R., Paresce, F., Beckert, T., & Weigelt, G. 2004, *A&A*, 418, L39
 Zheng, W., Kriss, G. A., Telfer, R. C., Grimes, J. P., & Davidsen, A. F. 1997, *AJ*, 457, 469